TITLE

BDNF controls phosphorylation and transcriptional networks governing cytoskeleton organization and axonal regeneration

AUTHORS

Vargas, J.N.S.,[1,2*] Brown, A.L.,[1*] Sun, K.,[1,2] Hagemann., C.,[2,3,6] Geary, B.,[4] Villarroel-Campos, D.,[1,2] Bryce-Smith, S.,[1] Zanovello., M.,[1] Lombardo, M.,[1] Ryandov, E.,[1] Stepic, A., Meysman, L.,[1] Majewski, S.,[1] Tosolini, A.P.,[1] Secrier, M.,[5] Keuss, M.J.,[1] Serio, A.,[2,3,6] Sleigh, J.N.,[1,2] Fratta, P.,[1,6] Schiavo, G.[1,2]

AFFILIATIONS

1. Department of Neuromuscular Diseases and UCL Queen Square Motor Neuron Disease Centre, UCL Queen Square Institute of Neurology, University College London, London, UK 2. UK Dementia Research Institute, University College London, London, UK. 3. Department of Basic and Clinical Neuroscience, King's College London, London, UK. 4. MRC Protein Phosphorylation and Ubiquitylation Unit, School of Life Sciences, University of Dundee, Dow Street, Dundee DD1 5EH, Scotland, UK. 5. Department of Genetics, Evolution and Environment, UCL Genetics Institute, University College London, London, UK. 6. The Francis Crick Institute, London NW1 1AT, UK. *These authors contributed equally. Correspondence: jobert.vargas@ukdri.ac.uk & giampietro.schiavo@ucl.ac.uk

SUMMARY

Axonal degeneration underlies neuromuscular disorders and neuropathies. Dysregulation of neurotrophic factors, such as brain-derived neurotrophic factor (BDNF), in the peripheral nervous system has long been established to exacerbate axonopathy. However, the molecular programs controlled by BDNF that facilitate axonal regeneration and transport are not well-understood. Here, we unravel the transcriptomic and phosphorylation landscape shaped by BDNF in human iPSC-derived motor neurons. Using SLAM-Seq, we reveal BDNF stimulation increases global transcription rate in motor neurons and governs gene regulatory networks that converge with those engaged during axonal repair/outgrowth. Phosphoproteomic analyses demonstrate that BDNF remodels the phosphorylation landscape of cytoskeletal-binding proteins, especially of structural microtubule-associated proteins. Importantly, the localized axonal-specific activation of ERK1/2 is necessary for BDNF to enhance axonal transport of neurotrophin-containing signaling endosomes and to potentiate axonal regeneration after axotomy. Collectively, this work unveils a novel molecular paradigm that positions BDNF as a core regulator of transcriptional and phosphorylation programs driving axonal regeneration and transport in human motor neurons.

HIGHLIGHTS

- SLAM-seq reveals increased global transcriptional rate by BDNF in human motor neurons
- BDNF modulates transcriptional programs that potentiate axonal outgrowth/regeneration
- BDNF governs the phosphorylation landscape of cytoskeletal-binding proteins
- Axonal BDNF-ERK1/2 signaling controls axonal transport and axonal regeneration

INTRODUCTION

Brain-derived neurotrophic factor (BDNF) signaling is essential for neuronal development and plasticity [1], and is crucial for motor neuron axon development and neuromuscular junction (NMJ) maintenance in the peripheral nervous system[2]. Peripheral nerve regeneration involves neuron-intrinsic signaling, as well as extrinsic cues from neurotrophins [3–6]. Dysfunctional neurotrophic support is an underpinning pathomechanism for motor neuron diseases and peripheral neuropathies [3–5]. Activation of tropomyosin receptor kinase B (TrkB) by BDNF stimulates multiple downstream kinases, most notably ERK1/2 and AKT, and activates gene transcription to drive pro-survival and pro-regenerative effects [7–10]. Previous work in mice revealed that BDNF enhances axonal regeneration in the periphery [11–13]. However, the mechanisms responsible for this effect are unclear. One of the main reasons for this knowledge gap is that to date, an in-depth exploration of the RNA dynamics controlled by BDNF in motor neurons is still lacking. Central and peripheral nerve injury activates combinatorial transcriptional networks through transcription factors that drive the expression of "regeneration-associated genes" (RAGs)[3,4,14–20]. Crucially, the upstream regulators of these regeneration-associated transcription factors and genes, particularly those driven by BDNF, remain undetermined.

Another crucial gap in our understanding of BDNF signaling is that the phospho-substrates downstream of TrkB activation, particularly in human motor neurons, are largely unexplored. BDNF plays a role in modulating the morphogenesis of several neuronal sub-compartments, including dendrites, axons, growth cones, and synapses, all of which depend on cytoskeletal remodeling [1,21,22]. However, the mechanisms by which BDNF accomplishes the *en masse* reorganization of the cytoskeletal network to control neuronal morphology are not completely understood. Axonal regeneration requires dynamic restructuring of the actin cytoskeleton as well as the microtubule network [23–25]. The organization and function of the latter is, in part, dictated by structural microtubule-associated proteins (MAPs)[26]. MAPs link cytoskeletal components with organelles, membranes, and with other cytoskeletal components; and control microtubule recruitment and activity of motor complexes. Phosphorylation of MAPs is a well-established paradigm for the regulation of microtubule-related processes[27], and this "MAP phosphorylation code" has been suggested to determine their spatiotemporal regulation.

In this study, we aim to unravel the effects of BDNF pertinent to axonal homeostasis in human motor neurons. We performed unbiased metabolic transcriptomics and tandem mass tagging (TMT)-phosphoproteomics, as well as functional assays on axonal transport and regeneration. We resolve the RNA dynamics driven by BDNF using thiol(SH)-linked alkylation for the metabolic sequencing of RNA (SLAM-seq)[28]. We uncover that the transcription factors activated by BDNF in motor neurons strikingly overlap with those that promote axonal outgrowth and regeneration. Crucially, our phosphoproteomic analysis delineated a novel function of BDNF in reshaping the phosphorylation state of various cytoskeletal-binding proteins, especially of MAPs. Finally, we demonstrate that BDNF fosters both axonal transport of signaling endosomes and regeneration through localized ERK1/2 signaling within axons of human motor neurons. Overall, this work reveals the underlying transcriptional and phosphorylation networks governed by BDNF potentially underpinning axonal transport and regeneration in human motor neurons.

RESULTS

BDNF signaling in human iPSC-derived motor neurons

We aim to explore the transcriptional programs and phosphorylation networks driven by BDNF in human motor neurons. To this end, we used the genetically-engineered human iPSC-derived lower motor neurons (i^3 LMNs) expressing *NGN2*, *ISL1*, and *LHX3* under a doxycycline-inducible promoter [29]. i^3 LMNs differentiate efficiently and are highly scalable, thus conducive for multi-omic analyses (**Fig. 1A;S1A**).

Post-differentiation, i^3 LMNs express ChAT and Hb9, two canonical motor neuron markers (**Fig. 1B-C**). Next, we sought to validate the signaling pathways activated by BDNF in the i^3 LMNs. Transient treatment of BDNF after growth factor deprivation resulted in the activation of ERK1/2, AKT, and S6K, indicating that PI3K/AKT and MAPK pathways are activated by BDNF in these neurons (**Fig. 1D**). We find that BDNF induces the ERK1/2-dependent phosphorylation of the canonical transcription factor CREB (**Fig. 1E**), as well as the transcription of an extensively studied BDNF early response gene, *FOS* (**Fig. 1F**). Furthermore, BDNF also induces the AKT-dependent phosphorylation of TSC2, which is inhibited by the AKT inhibitor ipatasertib (**Fig. 1G**). Immunofluorescence imaging of an axonal marker SMI-31 in i^3 LMNs cultured in microfluidic devices revealed robust axonal outgrowth (**Fig. 1H; S1B-C**).

We next compared the somatic and axonal activation of ERK1/2 and AKT in response to BDNF in motor neurons. For this comparison we cultured the i^3 LMNs on a microfabricated culturing platform combining soft lithography and 3D printed molds (SOL3D)[30], which has been developed specifically to study axonal biology [31] (**Fig. 1I**). The SOL3D fabricated devices allow for the efficient isolation of axonally-enriched material with significantly larger yield than other microfluidic systems, enabling biochemical assays. Western blot analysis reveals somatic- and axonal-enriched compartmentalization using SOL3D (**Fig. 1I-J**). After 1 h of treatment, we found BDNF activates ERK1/2 in both somatic and axonal compartments, whilst phosphorylated AKT levels are higher in somatodendritic compartment compared to axons (**Fig. 1J**). These data suggest that BDNF activates canonical ERK and AKT kinase pathways in i^3 LMNs and reveals a preferential activation of ERK1/2 by BDNF in axons of i^3 LMNs.

BDNF-driven transcriptional responses in motor neurons are temporally regulated

We used SLAM-seq (**S**H-**l**inked **a**lkylation for the **m**etabolic sequencing of RNA) in i^3 LMNs (**Fig. S2A**). SLAM-seq simultaneously measures RNA abundance and RNA transcription through the incorporation of 4-thiouridine (4sU) into nascently transcribed RNA. [28,32,33].

Principal component analyses on total RNA (PCA) revealed clear separation between BDNF-treated and control samples, with immediate early response genes, such as *EGR1, FOS*, *JUNB*, and *ARC* being the most important drivers of variance (**Fig. 2A-C**). BDNF significantly changed both gene expression and splicing of genes at 1 h (58 genes; 268 genes), 2 h (2,131 genes; 286 genes), and 6 h (604 genes; 245 genes); adjusted p-value < 0.1, abs (log2Fold change) > 0.75 - probability of delta percent spliced in (PSI) >= 20% > 90% (**Fig. S2B-D**; **Table. S1,S2**).

To identify genes showing coherent temporal-functional relationships upon BDNF signaling in motor neurons, we used hierarchical clustering on the fold-change of total RNA expression. We delineated sixteen expression clusters based on the fold-change after 1, 2, and 6 h of BDNF treatment and performed gene-ontology (GO) enrichment on each cluster (**Fig. 2D; Table S3**). We find distinct BDNF-driven functional clusters, such as extracellular matrix genes, presynaptic membrane, and ribosomal constituents, which behave differently across time (**Fig. 2D)**. Expectedly, immediate early response genes (clusters 13 and 16), showed rapid upregulation across all time points with a slower rate of increase at 6 h (**Fig. 2D**). GO analysis across BDNF treatment timepoints further revealed a time-dependent functional specificity downstream of BDNF treatment (**Fig. 2E**). We found expression of homeostatic feedback regulators of MAPK signaling, dual specificity phosphatase (DUSP) family and SPRY family, which spiked at 1 h. Extracellular matrix genes, and actin-binding with cell-cell adhesion genes dominated at 2 and 6 h (**Fig. 2E**; **S2B-D**; **Table S3**). We thus revealed the temporal behavior of various BDNF-responsive genes, offering a deeper insight into critical windows of BDNF responsive gene expression in motor neurons.

Given the known function of BDNF in transcription and the diverse processes we revealed from our GO analyses, we posited that multiple transcription factors may be mobilized by BDNF signaling in human motor neurons. We used gene set enrichment analysis (GSEA) in tandem with the DoRothEA database,

which curates benchmarked transcription factor-target gene interactions (**Fig. 2F**)[34]. Remarkably, BDNF genes are enriched for transcription factors reported to trigger neuron-intrinsic regeneration pathways in response to axonal injury [3,10,35] We found known BDNF-responsive genes are significantly enriched for the transcription factors STAT3 [36], TP53 [37,38], CREB [39], ELK1 [40], SP1 [14], SRF [41], ETS1[42], and Jun [43,44] (**Fig. 2F**). Interestingly, ATF3, which is also rapidly upregulated by BDNF (**Fig. S2B**), has been found to synergistically act with Jun, STAT3, and SP1 during neuronal damage [45] and is a critical transcription factor for nerve injury response [20,46,47]. Our transcription factor enrichment analysis reveals BDNF signaling may exert control over multiple injury-inducible transcription factors crucial for axonal outgrowth and regeneration.

SLAM-seq reveals BDNF impacts both transcription rate and RNA stability

We next investigated BDNF-dependent transcription kinetics with SLAM-sequencing. The direct readout of transcription during SLAM-seq – converted reads (reads with at least 2 characteristic T>C mismatches) – rose with 4sU labeling time in both control and BDNF samples, and BDNF samples had significantly more converted reads by 6 h (**Fig. 3A**). PCA on converted reads showed distinct clustering of treatment groups (**Fig. 3B; S3A)**. To assess transcription rate differences between control and BDNF-treated samples, we calculated their respective new-to-total RNA ratio (NTR; **Fig. S3B**). Remarkably, BDNF induced a global increase in transcription rate, especially from 2 and 6 h (**Fig. 3C**). Counterintuitively, this global increase in transcription did not correspond with a rise in total RNA abundance (**Fig. 3D-E**).

Overall, most genes were not significantly changed at the total RNA level upon BDNF treatment (**Table S1**); however, after 2 h of BDNF treatment, we found that the vast majority of genes that passed the strict NTR cutoff [48] (90% credible interval < 0.2) (**Fig. S3B**) had a higher new RNA ratio (1 h - 1,392 of 6,169 genes; 2 h - 6,858 of 8,835 genes; 6 h - 8,246 of 8,909 genes; **Fig. 3C-E)**. This suggests a novel function of BDNF in altering the baseline transcriptional output of human motor neurons, while concomitantly exerting homeostatic control over total RNA abundance. To the best of our knowledge, this is the first time a neurotrophin, such as BDNF, has been demonstrated to alter global transcription rate in neurons.

Next, we sought to understand the kinetics of BDNF-driven gene expression in motor neurons. By categorizing genes based on RNA abundance and NTR through a Monte-Carlo sampling (**Fig. 3E; S3B**), we unveiled gene regulation patterns driven by BDNF. For instance, genes displayed patterns of stabilization (upregulated, equivalent or lower new RNA; 1 h - 4 genes; 2 h - 123 genes; 6 h - 4 genes), destabilization (downregulated, higher new RNA; 1 h - 0 genes; 2 h - 306 genes; 6 h - 57 genes), and transcription (upregulated, higher new RNA; 1 h - 26 genes; 2 h - 61 genes; 6 h - 177). This diverse RNA regulation, along with an increase in transcription rates without a corresponding rise in RNA abundance, indicates that BDNF regulates gene expression through transcriptional, decay, and stability mechanisms. The optimal temporal expression of RNA relies on the coordination of all these RNA regulatory mechanisms [49]. Thus, we show a novel role of BDNF in controlling several aspects of RNA metabolism.

We were struck by a set of RNAs that were downregulated, yet paradoxically highly transcribed at 2 h post-BDNF treatment (**Fig. 3E; Table S1;** 306 genes). In this category were genes in pathways important for axonal regeneration such as axonal outgrowth, cytoplasmic translation[50], and the Wnt signalling pathway [51] (**Fig. S3C)**. We were also surprised that BDNF led to profound RNA degradation at 2 h, so we sought another comparable study that treated GABAergic neurons with BDNF for 2 h [52] . Despite the difference in neuron subtype, we found good correlation between the data sets (**Fig. S3D**; Spearman's rho = 0.43, p.value < 0.001), with 1,442 genes downregulated in the GABAergic dataset after 2 h BDNF treatment (adjusted p-value < 0.1, log2Fold change < -0.75), and significant overlap in the downregulated genes at 2 h (119 overlapping genes, p.value < 0.001, hypergeometric test). This indicates that BDNF may indeed drive RNA degradation in neurons, although the function of this is currently unknown.

BDNF regulates gene sets associated with axonal regeneration and outgrowth

We next performed GO enrichment according to the effect of BDNF on total RNA and new RNA fraction across treatment timepoints and found various functional gene sets (**Fig. 3F**). For instance, stabilized RNAs (increased total RNA without change in NTR) were enriched for extracellular matrix genes, which are critical for nerve regeneration[53] **(Fig. 3F; 2D)**. Intriguingly, at the same time point, genes encoding structural constituents of ribosome showed a downregulation in total RNA abundance, but a paradoxical upregulation in the NTR, suggesting that ribosomal genes are highly transcribed, but are also being degraded/destabilized (**Fig 3F; 2D**). Translation increases RNA destabilization[54] and BDNF stimulates the translation of ribosomal components[55] potentially leading to their instability.

Finally, to understand how BDNF treatment affects transcriptional programs associated with neuronal injury, we performed gene set enrichment analysis (GSEA) across three unique neuronal regeneration gene sets[14,16,20] on the abundance and transcriptional rate changes induced by BDNF (**Fig. 3G; S3E)**. At 1 h, genes in all three datasets showed increased transcriptional rate, as well as an increase in RNA abundance (**Fig. 3G; S3F**), suggesting BDNF rapidly upregulates the transcription of genes critical for neuronal injury response. However, the relationship of BDNF-driven genes at 2 h and 6 h with the three regeneration datasets is more complex, with genes downregulated by BDNF showing enrichment. (**Fig. 3G; S3F).** These data suggest BDNF rapidly regulates a diverse set of genes crucial for neuronal injury response, potentially priming cells for effective nerve repair *a priori* of injury. This is in line with previous reports whereby axonal regeneration enhancers exert transcriptional responses prior to injury that potentiates the regenerative capacity of axons [16,20].

BDNF reshapes the phosphorylation landscape of cytoskeletal-interacting proteins in human motor neurons.

Another important component of BDNF signaling in neurons is the activation of downstream kinases through TrkB activation. We therefore probed the phosphoproteomic events driven by BDNF signaling on i^3 LMNs through tandem mass tagging (TMT) quantitative phosphoproteomics. We treated the i^3 LMNs 1 h or 6 h with BDNF after 2 h of growth factor withdrawal (**Fig. 4A; Table. S4**). At both timepoints, NTRK2/TRKB is the most phosphorylated protein identified, along with the well-established signaling nodes expected to be activated by BDNF, such as TSC2 and MAP2K1/MEK1 (**Fig. 4B,C**). We identified 148 significant phosphorylation hits at 1 h and 49 hits at 6 h (adjusted p-value < 0.1 & abs(log2FC) > 0.5).

Remarkably, we discovered profound alterations in the phosphorylation state of several cytoskeletal-binding proteins downstream of BDNF signaling (**Fig. 4B-G; S4A-D, G, H**). Indeed, many microtubule-associated proteins (MAPs) were phosphorylated and dephosphorylated at various sites (**Fig. 4B,C; S4A-D, H**). For instance, MAP1A is phosphorylated at S499 and dephosphorylated at S2019 and S2022 (**Fig. 4B**). MAP1B, on the other hand, is phosphorylated at S995, S992, S1265, S1520, and dephosphorylated at S1408 and T744 at 1 h of BDNF treatment, indicating complex kinetics of phosphorylation of MAPs. (**Fig. 4B**). MAP7D1 is phosphorylated at S460 only at 1 h of BDNF and is exclusively dephosphorylated at T118 at 6 h of BDNF treatment, indicating distinct temporal responses of certain MAPs to BDNF. In support of this notion, the minus-end binding MAP, CAMSAP3 is phosphorylated at S341 and dephosphorylation at S1074 primarily at 1 h, but not 6 h (**Fig. 4B,C**). The microtubule-actin crosslinking protein CLASP1 is only phosphorylated at 1 h of BDNF treatment, but not after 6 h. Indeed, many phosphorylation events on MAPs occur at 1 h and dissipate by 6 h, suggesting a rapid response of cytoskeletal components to BDNF followed by a potential negative feedback regulation. Other notable phospho-events on MAPs that we identified include the actin-microtubule crosslinking

protein MACF1 (S1378), microtubule-destabilizing protein STMN1 (S25), MAP2 (T1602, T1605, S788, S821), plus-end microtubule-binding proteins MAPRE1/EB1 (S155) and CLASP2 (S1209, T1279.)

It is worth mentioning that various actin-binding proteins, such as IQGAP2, PALLD, MPRIP, and MLLT4 are also phospho-substrates of BDNF signaling. Furthermore, we identified the kinesin motor protein KIF21A as a top hit downstream of BDNF (**Fig. 4B, C; S4G, H**). As a proof of principle of the reliability of our analysis, we validated the phosphorylation of two of our hits, STMN1 and LIN28A, by western blot (**Fig. S4I, J**). STMN1 is dynamically expressed in regenerating axons and accumulates in axons after injury[56]. LIN28A is also regulated by BDNF at the RNA level (**Fig. S2B**) and recent studies show that LIN28A positively regulates axonal regeneration [57–59].

Functional network prediction reveals BDNF regulates phosphorylation of cytoskeleton-interacting proteins

We performed unbiased functional enrichment analyses on the significant BDNF-dependent phospho-events in i^3 LMNs. We reveal an overrepresentation of the microtubule polymerization and depolymerization pathways at 1 h of BDNF treatment, indicating the regulation of microtubule dynamics by BDNF (**Fig. 4D**). Accordingly, axonogenesis, neurite projection, and regulation of intracellular transport GO processes that depend on cytoskeletal reorganization, are the pathways enriched at 6 h of BDNF treatment (**Fig 4E**). We generated gene-concept networks to further visualize the functional networks involved in BDNF phospho-signaling (**Fig. 4F, G, Fig. S4A-D**). We found that cytoskeletal organization and synonymous functional taxonomies were regulated by BDNF at 1 and 6 h (**Fig. 4F, G; Fig. S4A-D**). Interestingly, the gene-concept networks also identified various signaling nodes with well characterized functions on the neuronal cytoskeleton. For example, BRSK1 has known roles in neuronal polarity via Tau phosphorylation [60,61]. Furthermore, the kinase RPS6KA3/RSK2 has recently been reported to enhance axonal regeneration [62]. Other pathways enriched by BDNF-driven phosphorylation events are the regulation of MAPK/ERK signaling, translation initiation factor binding, mRNA binding, and transcription coregulation activity (**Fig. S4G**).

Taken together, these data demonstrate that BDNF governs the dynamic phosphorylation of various microtubule- and actin-binding proteins.

BDNF-dependent phosphorylation events on cytoskeletal components are predominantly within proline-directed serine motifs

Our functional enrichment analyses detected serine phosphorylation as a core pathway activated by BDNF (**Fig 4D-G, Fig. S4A-D**). This prompted us to investigate the phosphorylation motifs downstream of BDNF. We generated a sequence logo [63] of all the significant phosphopeptides identified, and found that BDNF treatment primarily resulted in phosphorylation of serines followed by a proline at the +1 position (*p*S/T-P; **Fig. 4H; S4E, H; Table. S4**). Proline-directed kinase families include mTOR, cyclin-dependent kinases, and MAPK/ERK. Indeed, the STMN1 and LIN28A BDNF-dependent phosphosites that we validated by western blot analysis were both proline-directed and required ERK1/2 activity (**Fig. S4I, J**). Although not as pronounced as pS-P, the basophilic RXRXX*p*S/T (X = any amino acid) phospho-motif canonical to the AGC superfamily kinases [64] is also evident in our motif analysis (**Fig. 4H; S4E**). Using exclusively the serine with a +1 proline phosphosite as inputs for Cytoscape StringApp analysis revealed an enrichment of cytoskeletal-binding proteins (**Fig. 4I**). Although the RXRXXpS/T phosphorylated residues did not exhibit enrichment for cytoskeleton regulatory pathways, a number of the actin and microtubule-binding protein hits, such as IQGAP2, MAP2, and CLASP1, exhibit BDNF-dependent phosphorylation on this motif (**Fig S4H**). These data suggest that BDNF modulates cytoskeletal components via phosphorylation mainly through conserved proline-directed serine residues, and to a lesser degree, serines within the AGC motif.

BDNF activates several kinases in iPSC-derived motor neurons

Next, we sought to identify kinases activated by BDNF in human motor neurons. To do so, we used a kinase prediction tool based on a recent study that used large-scale combinatorial synthetic peptide libraries to profile the substrate sequence specificity of more than 300 kinases [65]. Using the phospho-peptides we identified as inputs, we reveal kinases that are enriched in our hits**.** Of note, RSK family kinases had the highest kinase enrichment scores followed by S6 kinases (**Fig 4J- S4F**). These kinases belong to the AGC family and are known to be activated downstream of the MAPK/ERK pathway [64,66]. Recent work showed that RSKs determine intrinsic axonal regeneration propensity [62,67] suggesting that activation of this pathway by BDNF could potentiate axonal regrowth. Indeed, our kinase predictions are in line with the logo seq motif analysis (**Fig. 4H; S4E**). Interestingly, a handful of phospho-motifs are reduced after 6 h of BDNF treatment. This group is enriched in kinase motifs relating to p38α, EEF2K, and ERK1 indicating a negative feedback regulation of the MAPK pathway at the phospho-enrichment level upon prolonged BDNF treatment (**Fig. S4F**), similar to the negative feedback loop in MAPK signaling we observed at the transcriptional level (**Fig. S2B-D**). Importantly, a previous chemical screen showed that inhibition of p38α corrected axonal transport defects in a mouse model of amyotrophic lateral sclerosis (ALS) [68].

Overall, our phosphoproteomic and bioinformatic analyses reveal that BDNF reshapes the phosphorylation landscape of several cytoskeletal-interacting proteins in motor neurons.

BDNF increases axonal transport of signaling endosomes through ERK1/2 signaling

Regulation of the cytoskeletal network can directly impact axonal transport. Given the role of BDNF in global phospho-regulation of cytoskeleton-interacting proteins (**Fig. 4**), we set out to test whether BDNF alters axonal transport dynamics in human motor neurons. To this end, we cultured the i^3 LMNs in tripartite microfluidic chambers (MFCs) and monitored the transport dynamics of neurotrophic signaling endosomes (SEs) visualized with the fluorescently-labeled atoxic fragment of tetanus neurotoxin [69] (**Fig. 5A-B**). Since the addition of BDNF to i^3 LMNs caused a sustained activation of ERK1/2 in both soma and axons, whilst AKT activation occurred mostly in the soma (**Fig. 1H-I**), we decided to focus on the role of BDNF and ERK1/2 in axonal transport. We first tested the localized activation of ERK1/2 by BDNF using MFCs and showed that BDNF activates ERK1/2 in axons. Crucially, this activation is completely blocked by the co-treatment of i^3 LMN with BDNF and the ERK1/2 inhibitor U0126 (**Fig. 5B**).

Treatment of axonal terminals with BDNF is sufficient to increase the retrograde transport velocity of SEs, as assessed using Kymoanalyzer [70] (**Fig. 5C**). We are able to recapitulate this effect in primary mouse motor neurons (**Fig. S5A-F**) consistent with our previous findings [71]. Interestingly, in primary mouse motor neurons, inhibition of AKT resulted in increased retrograde transport of SEs [72]. Critically, we reveal that the BDNF-dependent increase in axonal transport of SEs is completely reversed if ERK1/2 signaling is inhibited by U0126 (**Fig. 5D**). ERK1/2 inhibition also increased the pausing frequency of SE even in the presence of BDNF (**Fig. E,F**). Both BDNF and ERK1/2 inhibition had no effect on the directionality of SEs (**Fig. 5G-H**), nor in pause duration (**Fig. S5G-H**).

We previously demonstrated that local injection of BDNF into the gastrocnemius and tibialis anterior muscles, or viral-mediated overexpression of BDNF in these muscles, upregulates the velocity of SE in intact sciatic nerve axons *in vivo* [71,73]. Here, when an ERK1/2 inhibitor, refametinib, is injected into tibialis anterior muscles with virally-enhanced BDNF levels, the previously observed BDNF-mediated increase in SE transport is abrogated (**Fig. S5 I-J**).

These results indicate that BDNF fosters axonal transport of SEs through the subcellular activation of ERK1/2 within axons of human and mouse motor neurons.

BDNF enhances axonal regeneration in human motor neurons through ERK1/2

Based on the BDNF-mediated phosphorylation of cytoskeletal-binding components and enhancement of axonal transport (**Fig. 4 and 5**), we asked whether BDNF drives posttranslational modifications of tubulin itself. These modifications have been shown to profoundly affect the architecture of the cytoskeletal network [24] and are dynamically modulated during axonal regeneration [23]. Our biochemical analysis on motor neuron lysates revealed that neither BDNF nor ERK1/2 inhibition altered levels of tyrosinated, acetylated, or polyglutamylated microtubules (**Fig. S6A**). Interestingly, at the subcellular level, axonal-specific inhibition of ERK1/2 affected the ratio of tyrosinated versus acetylated microtubules at the proximal and distal axon (analyzed axon spanning from 50 µm to 40 µm away from the tip (proximal) and the last 10 µm towards the tip (distal); **Fig. S6B-D**). These results suggest that although loss of ERK1/2 activity alters the detyrosinated/acetylated tubulin ratios regionally in motor neuron axons, BDNF signaling is not directly affecting this process.

Our transcription factor enrichment analysis revealed that BDNF regulates injury-responsive transcription factors (**Fig. 2F**), as well as genes that are upregulated during axonal injury (**Fig. 3G**). Thus, we aimed to test the role of BDNF and ERK1/2 in axonal regeneration. To this end, we performed axotomy experiments using i^3 LMNs cultured in tripartite MFCs (**Fig 6A**). After axotomy, we allowed axons to regenerate for 48 h in the presence of media without growth factors, or media with BDNF alone or with ERK1/2 and AKT inhibitors (**Fig. 6A**). We demonstrate that BDNF increases the axonal regeneration of motor neurons (**Fig. 6B**). Crucially, we also reveal that the potentiation of axonal regeneration mediated by BDNF necessitates functional ERK1/2 in axons (**Fig. 6C**). This is in line with our proteomics data suggesting that top putative kinases activated by BDNF, such as RSKs, are downstream of ERK1/2 (**Fig. 4)**. Since inhibition of axonal ERK1/2 resulted in the almost complete inhibition of axonal regeneration, these data also indicate that ERK1/2 have BDNF-independent roles in axonal repair mechanisms. Furthermore, inhibition of axonal AKT did not block BDNF-dependent axonal regeneration (**Fig. 6D**), suggesting axonal activity of AKT is dispensable for this BDNF function in i^3 LMNs. Interestingly, a screen to identify axonal regeneration promoting compounds in iPSC-derived motor neurons found that AKT inhibitors enhanced neurite outgrowth [74].

Taken together, these results show that BDNF potentiates axonal regeneration of human motor neurons through local axonal activation of ERK1/2.

DISCUSSION

While the role of BDNF in regulating axonal regeneration is well-documented in mouse models, and despite on-going exploration of neurotrophins as therapeutic tools to hasten axonal regeneration [75–77], a comprehensive understanding of how BDNF impacts human motor neurons is lacking. This work begins to fill this crucial gap by revealing novel molecular insights into the specific transcriptional and phosphoproteomic dynamics driven by BDNF in human motor neurons.

To assess in-depth the transcriptomic programs triggered by BDNF in motor neurons, we used SLAM-seq and found a striking global increase in transcriptional rate. This massive upregulation of transcription is not reflected in total RNA levels. Furthermore, we discovered a complex spatiotemporal regulation of RNA metabolism triggered by BDNF. Indeed, various functionally distinct BDNF-dependent RNA regulatory networks displayed stabilization and degradation behavior patterns. These novel findings raise the possibility of a post-transcriptional regulation through BDNF that impacts the turnover of a vast array of RNAs, whilst initiating widespread increase in transcription. Previous work in mitotic cells using

SLAM-seq showed that forced nuclear localization of Myc can also increase global transcriptional burst rates [78]. Further studies are required to pinpoint the underpinning mechanisms of the complex RNA regulation by BDNF.
We revealed that BDNF coordinates transcriptional programs that overlap with pro-regenerative RNAs in response to injury through GSEA. Using a well-established transcription factor-target RNA regulatory network database, we also identified BDNF-activated transcription factors, many of which were demonstrated to enhance axonal regeneration. Thus, BDNF may act as upstream activator of injury-responsive gene networks, consistent with the potency of BDNF in axonal repair[77]. It is critical to note here that the sequencing analyses we performed did not involve experimentally inducing axonal injury. The overlap of BDNF-driven transcripts with injury-responsive RAGs [14,16,17] indicates that BDNF signaling confers a priming or pre-conditioning effect at the transcriptional level, allowing motor neurons to respond more promptly to axonal injury.

BDNF controls the cytoskeletal architecture of various neuronal compartments, such as dendritic spines, axons, and growth cones [22,79]. Our phospho-proteomics delving into BDNF-dependent substrates in motor neurons revealed a striking enrichment of cytoskeletal components. We reveal that BDNF drives the phosphorylation of structural MAPs, such MAP1A/B, MAP7D1, and MAP2 and actin-binding proteins, modifying them at multiple sites.

Various molecular components playing major roles in focal adhesion, growth cone and axonal dynamics [23,80], are phospho-substrates of BDNF signaling. For instance, we found that CLASPs, as well as MAPRE1/EB1, are phosphorylated downstream of BDNF. These proteins form a complex at the microtubule plus-end tips in a phosphorylation-dependent manner and contribute to axonal extension[80]. Actin-binding proteins IQGAP2, PALLD and the microtubule-actin crosslinking protein MACF1 are also phosphorylated upon BDNF incubation. These suggest that BDNF plays a role in coordinating actin-microtubule crosstalk in motor neurons, a process that is required for the integrity of axons[81]. Many of the phospho-sites we identified on cytoskeletal-binding proteins have not yet been functionally characterized. MAPs are postulated to not only alter microtubule architecture, but also the recruitment of motor proteins and act as contact points with other cytoskeletal components [24,26,27]. The phosphorylation of MAPs may provide an additional layer of regulatory control for their function [27]. Important advances in experimental methods probing the biophysical properties of MAPs may further elucidate the roles of these novel phospho-sites on microtubule dynamics through phospho-mimetic/-deficient mutations [82].

Taken together, we demonstrate that BDNF is a central node for integrating neurotrophic signaling with the phospho-regulation of cytoskeletal-binding proteins. Further work is now needed to validate the axonal specificity of the phospho-events identified herein. It is reasonable to posit that the cytoskeletal protein phosphorylation events driven by BDNF may also be important for other neuronal subcompartments.

We provide functional data demonstrating that BDNF potentiates axonal transport and regeneration through the local activation of ERK1/2 in human motor neurons. It is crucial to note here that both ERK1/2 and AKT activity are important for axonal outgrowth/regeneration in various experimental models. For instance, ERK1/2 is activated upon sciatic nerve crush and inhibition of ERK1/2 prohibits axonal regeneration [83]. Lentiviral overexpression of TrkB in layer V corticospinal neurons enables adult axonal regeneration through ERK1/2 [84]. AKT inhibits death and accelerates axonal regeneration of hypoglossal motor neurons [85]. Deletion of PTEN, an upstream inhibitor of the AKT pathway, increases axonal regeneration of mouse retinal ganglion cells [86,87] and corticospinal neurons [84,88]. How the myriad of kinase pathways impacted by neurotrophins in neurons exerting their role in axonal regeneration will require further disentangling at the phospho-substrate level, which will also partially depend on the neuronal subtypes being examined.

Signaling endosomes (SEs) are critical for the long-distance retrograde transmission of neurotrophins, which once in the soma, drive the expression of prosurvival genes [8,21,73,89,90]. Here, we have demonstrated that BDNF enhances the retrograde axonal transport of SEs through ERK1/2 in human motor neurons, suggesting that the BDNF/ERK axis has axonal-specific roles in enhancing transport. Previous work showed that dynein-mediated retrograde transport of axonally-activated ERK1/2 is required for peripheral nerve regeneration after injury [91]. It is tempting to speculate that locally activated ERK1/2 is able to hitchhike on SEs back to soma to switch on pro-survival programs. Our previous work showed that local muscle administration or viral overexpression of BDNF in muscles corrects axonal transport defects of SEs and pathological symptoms in peripheral neuropathy mouse models [73,92].

Altogether, this study resolves BDNF signaling networks in human motor neurons and provides critical insights for the fine-tuning of neurotrophin-based therapies aimed at ameliorating human axonopathies[93].

ACKNOWLEDGMENTS

We thank Prof. Dario Alessi (University of Dundee) for his support and access to mass spectrometry facilities. We would also like to thank Drs. Christopher Grunseich and Michael Ward (NIH/NIA) for kindly sharing the i^3 LMNs. We also thank Prof. Carsten Janke for the critical reading and comments of the manuscript.

DECLARATION OF INTEREST

The authors declare no conflicts of interest.

FUNDING

This project was funded by a Brain Research UK Fellowship award BF-100029 (JNSV); Motor Neuron Disease Association Junior Non-Clinical Fellowship Tosolini/Oct20/973-799 (APT); Medical Research Council award MR/S006990/1 (JNS); Wellcome Trust awards 107116/Z/15/Z and 223022/Z/21/Z (GS); and a UK Dementia Research Institute Foundation award UKDRI-1005 (GS).

AUTHOR CONTRIBUTIONS:

Conceptualization: JNSV. Investigation/Data generation: JNSV, ALB, KS, CH, DVC, MZ, ML, ER, AS, LM, SM, APT, JNS. Writing of the manuscript: JNV, ALB. Figure assembly: JNSV, ALB, KS. Editorial processing: GS, JNS, with the contribution of all authors. Supervision and funding: GS.

FIGURE LEGENDS

Figure 1. BDNF signaling in human iPSC-derived motor neurons i^3 LMNs

A) Schematic of i^3 LMNs differentiation.
B) Immunofluorescence imaging of i^3 LMNs for motor neuron markers ChAT and Hb9.
C) Western blot analysis of iPSC and differentiated i^3 LMNs for expression of ChAT.
D) Western blot analysis of i^3 LMNs after serum starvation for 30 min and BDNF treatment for 10 min (25 ng/mL).
E) Western blot analysis to test ERK1/2 signaling in i^3 LMNs (DIV7). Neurons were starved for 2 h and treated with 25 ng/mL of BDNF for 1 h with or without U0126 (20 μM)
F) RT-qPCR analysis of *FOS* mRNA expression in i^3 LMNs after BDNF treatment (25 ng/mL) with or without the transcriptional inhibitor, Actinomycin D (ActD). N=3; Two-way ANOVA.

G) Western blot analysis to test AKT signaling in i^3 LMNs. Neurons were starved for 2 h and treated with 25 ng/mL of BDNF for 1 h with or without Ipatasertib (0.1 μM).
H) Immunofluorescence of i^3 LMNs (DIV 12) cultured in tripartite microfluidic chambers. SMI-31 signal delineates the axonal compartment and MAP2 labels the somatodendritic compartment.
I) i^3 LMNs (DIV12) cultured in the SOL3D platform and fluorescently labeled with live cell tubulin marker SiR-tubulin. Scale bar = 1000 μm.
J) Western blot analysis of i^3 LMNs (DIV12) cultured in SOL3D. Protein lysates were obtained from somatic-enriched and axonal-enriched fractions. Neurons were starved for 2 h and then treated with 50 ng/mL BDNF for 1 h. Red asterisks - background.

All western blot analyses were performed at least N=2 biological replicates. Data are represented as mean ± SEM. p value: * = < 0.05; ** < 0.01; *** < 0.001; **** < 0.00001; ns., not significant. Scale bars: 50 μm, unless indicated otherwise.

Figure S1. Differentiation of iPSC-derived lower motor neurons and response to BDNF

A) Brightfield images of WTC11 iPSC at DIV1 and 3; and 7 DIV i^3 LMNs post-differentiation. Scale bars: 50 μm
B) Diagram for the tripartite MFCs. i^3 LMNs are seeded in the center compartment and axons are allowed to grow into the left and right axonal compartment. Scale bars: 50 μm
C) Confocal images of axons from i^3 LMNs cultured within the axonal compartment of tripartite MFCs. Arrows indicate the microgrooves.

Figure 2. Profiling the temporal dynamics of BDNF-dependent transcription in human motor neurons

A) Total RNA principal component analysis.
B–C) Gene loading plots for (A) showing the most important genes for the first 2 principal components.
D) Differential gene expression clustering across BDNF treatment time showing mean and individual gene cluster expression with cluster GO terms/gene names.
E) Gene-ontology analyses for up- and downregulated genes collapsed for semantic similarity.
F) Gene set enrichment analysis (GSEA) transcription factor (TF) regulons from DoRothEA. Red - TF activates target genes; blue - TF represses target genes. Positive TF enrichment scores - target genes upregulated. 6 h - ETS1 activated targets were significantly enriched.

Figure S2. BDNF treatment of human motor neurons causes widespread gene expression and splicing changes in human motor neurons

A) Schematic of SLAM-sequencing pipeline.
B-C) Volcano plots of differentially expressed genes with 1, 2, and 6 hours of BDNF treatment in i^3 LMN. Lines define cutoff for a gene being called as differentially expressed (adjusted p-value < 0.1, abs (log2Fold change) > 0.75). Y-axis is cut for genes with p-values approaching zero.

Figure 3. SLAM-sequencing uncovers the transcriptional response to BDNF in human motor neurons

A) Converted reads per million mapped at 1, 2, and 6 h of 4SU treatment in control and BDNF treated i^3 LMN.
B) Converted reads principal component analysis.

C) Transcriptome-wide distribution of the log2Fold change of condition specific (**Fig. S3B**) new-to-total(NTR) RNA fraction.
D) Transcriptome-wide distribution of the log2Fold change of total RNA.
E) Categorization of genes by BDNF's effect on total RNA abundance and NTR (**Fig. S3B)** across treatment times.
F) Gene-ontology enrichment for genes categorized in (F). No significant GO terms were found at 6 h treatment time. Significant GO terms using an adjusted p-value < 0.05.
G) Distribution of the log2Fold NTR and total RNA for axonal regeneration sets[14,16,20]. Color refers to the adjusted p-value of the gene-set enrichment analysis of that gene set. Enrichment scores in **Fig. S3F.** Significant GSEA with an adjusted p-value < 0.05.

Figure S3. SLAM-sequencing reveals differential effects of BDNF on total and new RNA

A) Gene loading plots for (Fig. 3B) showing the most important genes for the 2 principal components separating control and BDNF samples. Top, gene loadings for PC1, bottom gene loadings for PC2.
B) Schematic of Monte-Carlo sampling approach used to determine condition specific new-to-total RNA ratio (NTR). Beta-distributions on the NTR for a gene for each of N = 3 biological replicates at each time point were estimated by GRAND-SLAM [32]. Condition-specific beta distributions were created by merging the sample beta-distributions with each sample weighted inversely by its variance. Condition NTR was calculated by performing one million samples from each condition's beta distribution, and differential labeling was determined by comparing the difference between each of the 1 million samples.
C) Scatterplot showing the relationship between total RNA change and ratio between BDNF and control NTR for the genes downregulated at total level with higher NTR at 2 hours (dark blue genes in **Fig. 3E,** second panel, Downregulated). Genes have been colored by if they have biological relationship to axonal outgrowth (mint green) cytoplasmic translation (yellow), or the Wnt signaling pathway (pink).
D) Correlation between of the significantly differentially expressed genes after 2 hours BDNF treatment time in i^3 LMN with the log2Fold change in published RNA-seq with 2 hour BDNF treatment time on H9 human embryonic stem cell-derived GABAergic inhibitory neurons [52]. Spearman's correlation coefficient shown. Line drawn represents the line of best fit.
E) Number of genes and overlap between three different gene sets defining neuronal injury response. Gene sets are originally derived from Rattus norvegicus (PNS RAGs, Chandran 2016 [14]) and Mus musculus (Regenerating axons, Jacobi 2022 and Neuronal injury response, Renthal 2020 [20]) and were first mapped to their human orthologs using gprofiler[94].
F) Normalized enrichment score (NES) and adjusted p-value for the log2Fold Change of total RNA and NTR on neuronal injury response gene sets in E. Bolded and highlighted enrichments are significant at adjusted p-value < 0.05.

Figure 4. Global alterations of cytoskeletal-interacting proteins phosphorylation induced by BDNF in i3 LMNs

A) Schematic of tandem mass tagging phosphoproteomics. Unique isobaric tags were added to control, 1 h, and 6h BDNF-treated i^3 LMNs.
B-C) Volcano plot showing the fold change and adjusted p-values of the phosphorylation sites at 1 h (B) and 6 h (C) after BDNF (25 ng/mL) treatment . Each point represents a phosphosite. Blue dots represent microtubule associated proteins (MAPs). Significantly differentially phosphorylated sites in MAPs sites are labeled with protein name and significant site. Dotted lines represent adjusted p-value 0.1 and log2Fold change +/- 0.5.

D-E) Dotplot showing gene-ontology (GO) enrichment on genes with significant changes in phosphorylation at 1 h (D) and 6 h (E) after BDNF treatment.
F-G) Gene-concept networks depicting the gene-GO relationships for genes with significant changes in phosphorylation at 1 h (F) and 6 h (G) after BDNF treatment.
H) Sequence logo of differentially phosphorylated sites after 1 h BDNF treatment, height of letter displaying the frequency of the amino acid at each site.
I) Cytoscape StringdB network of BDNF-dependent proline-directed serine residues enrichment for cytoskeletal protein-binding (in yellow). Inputs peptides p-value > 0.05.
J) Kinase enrichment at 1 h after BDNF treatment based on site sequence of differentially phosphorylated sites. Dotted line shows significant enrichment at p-value < 0.01.

Figure S4. Microtubule- and actin-binding protein phosphorylation via BDNF in i^3 LMNs

A-B) Gene-concept networks depicting the gene-GO relationships at 1 h BDNF treatment for genes with significant upregulated phosphosites (A) and downregulated phosphosites (B). Significant sites called as adjusted p-value < 0.1.
C-D) Gene-concept networks depicting the gene-GO relationships at 6 h BDNF treatment for genes with significant upregulated phosphosites (C) and downregulated phosphosites (D). Significant sites called as adjusted p-value < 0.1.
E) Sequence logo of differentially phosphorylated sites after 6 h BDNF treatment, height of letter displaying the frequency of the amino acid at each site.
F) Kinase enrichment at 6 hours BDNF treatment based on site sequence of differentially phosphorylated sites. Dotted line shows significant enrichment at p-value < 0.01.
G) Gene-concept heatmap showing the overlap between significantly phosphorylated genes after 1 h BDNF treatment and the shared gene-ontology terms, highlighted in blue are the GO terms related to cytoskeletal organization.
H) Diagram of significant phosphorylation events on pS/TP and RXRXXpS/T motifs downstream of BDNF treatment on microtubule and actin-binding proteins.
I) Western blot analysis of phosphorylated STMN1 (S25) after BDNF treatment with or without U0126 (20 μM) for 1 h.
J) Western blot analysis of phosphorylated LIN28A (S200) after BDNF (25 ng/mL) treatment with or without U0126 (20 μM) for 1 h.

Figure 5. BDNF enhances retrograde transport and axonal regeneration through ERK1/2 in i^3 LMNs

A) Schematic of tripartite MFC and experimental design for live imaging of signaling endosome (SE) axonal transport in i^3 LMNs. (HcT = fluorescently-labeled atoxic fragment of tetanus neurotoxin)
B) Confocal images of immunofluorescent staining of ERK1/2 activation in i^3 LMNs cultured in tripartite MFCs. The entire MFC plate is starved for 1h. Axons were then treated with BDNF (25ng/mL) for 1h. For axons treated with the ERK1/2 inhibitor, U1206 20 μM is added to starvation media to pre-treat the axons. BDNF and fresh U1206 were then added for 1h.
C) Retrograde velocities of HcT-labeled SEs with or without BDNF (25 ng/mL) treatment.
D) Retrograde velocities of HcT-labeled SEs with or without co-treatment of BDNF (50 ng/mL) and U1026 (20 μM).
E) Pause frequency of SEs with or without BDNF treatment (25 ng/mL).
F) Pause frequency of SEs with or without co-treatment of BDNF (25 ng/mL) and U1026 (20 μM)..
G) Percent cargo population of SEs with or without BDNF (25ng/mL) treatment.
H) Percent cargo population of SEs with or without co-treatment of BDNF (25ng/mL) and U1026 (20 μM).

Data are represented as mean ± SEM. p value: ∗ = < 0.05; ∗∗ < 0.01; ∗∗∗ < 0.001; ∗∗∗∗ < 0.00001; ns., not significant. Scale bars: 50 µm, unless indicated otherwise. Paired t-test. Control vs BDNF N=5. control vs BDNF+ERKi N=4. Each N is an independent tripartite microfluidic culture.

Figure S5. BDNF and ERK1/2 regulates axonal transport of signaling endosomes in mice

A) Schematic of tripartite MFC and experimental design for live imaging of signaling endosome (SE) axonal transport using primary mouse motor neurons.
B) Western analysis of DIV7 primary mouse motor neurons with starvation and BDNF treatments.
C) Retrograde velocities of HcT-labeled SEs in primary mouse motor neurons with or without BDNF (25ng/mL) treatment.
D) Pause frequency of SEs in primary mouse motor neurons with or without BDNF (25ng/mL) treatment.
E) Pause duration of SEs in primary mouse motor neurons with or without BDNF (25ng/mL) treatment.
F) Percentage cargo population of SEs in primary mouse motor neurons with or without BDNF treatment (25ng/mL).
G) Pause duration of SEs with or without BDNF treatment (25ng/mL) using i^3 LMNs.
H) Pause duration of SEs with or without co-treatment of BDNF (25ng/mL) and U1026 (20 µM) using i^3 LMNs.
I) Schematic of experimental design of the in vivo imaging of SE transport in the sciatic nerve
J) Retrograde velocities of HcT-labeled SEs in mouse sciatic nerves with BDNF or BDNF with Refaminitinib (50 nM).

Data are represented as mean ± SEM. p value: ∗ = < 0.05; ∗∗ < 0.01; ∗∗∗ < 0.001; ∗∗∗∗ < 0.00001; ns., not significant. Scale bars: 50 µm, unless indicated otherwise. Paired t-test was used for *in vitro* transport. i^3 LMNs: Control vs BDNF N=5. control vs BDNF+ERKi N=4. Mouse primary motor neuron transport: N=6. Each N for in vitro experiments an independent tripartite microfluidic culture. *In vivo* axonal transport: 5 mice per condition; N=15 axons analyzed for BDNF with Refamitinib. N=12 axons for BDNF only condition.

Figure 6. BDNF and ERK1/2 regulates axonal regeneration of motor neurons

A) Experimental design of axotomy experiments.
B) Axonal density after axotomy and 48 h recovery with or without BDNF (25 ng/mL)
C) Axonal density after axotomy and 48 h recovery with or without co-treatment of BDNF (25 ng/mL) and U1206 (20 µM).
D) Axonal density after axotomy and 48 h recovery with or without co-treatment of BDNF (25 ng/mL) and the AKT inhibitor Ipatasertib (0.1 µM).
E) Representative confocal images of axons from C-D. i^3 LMNs are immunostained with β3 tubulin. Scale bars: 50 µm.

Data are represented as mean ± SEM. p value: ∗ = < 0.05; ∗∗ < 0.01; ∗∗∗ < 0.001; ∗∗∗∗ < 0.00001; ns., not significant. Paired t-test was used for *in vitro* transport. i^3 LMNs: Control vs BDNF N=4. Control vs BDNF+ERKi N=4. Control vs BDNF+AKTi N=5. Each N is an independent tripartite microfluidic culture.

Figure S6. Microtubule modifications in i3LMNs

A) Western blot analysis of tubulin posttranslational modifications in i^3 LMNs.
B) Confocal imaging of immunostained i^3 LMNs (DIV 12) for acetylated or tyrosinated tubulin in axons. Tyrosinated = magenta; acetylated = green. Scale bars = 50 µm
C) Graphs showing tyrosinated/acetylated tubulin immunostaining ratios at the proximal axon. Proximal axon is defined as an axonal segment spanning 10 µm, 40-50 µm away from the distal end. Axonal compartments were depleted of growth factors for 2 h and BDNF (25 ng/mL) and U1206 (20 µM) were added to the axonal compartment for 1 h.
D) Graphs showing tyrosinated/acetylated tubulin immunostaining ratios at the distal axon. Distal axon is defined as an axonal segment spanning 10 um from the extreme distal tip. Axonal compartments were depleted of growth factors for 2 h and BDNF (25 ng/mL) and U1206 (20 µM) were added to the axonal compartment for 1 h.

Two-way ANOVA. Data are represented as mean ± SEM. p value: * = < 0.05; ** < 0.01; *** < 0.001; **** < 0.00001; ns., not significant. N=4.

STAR METHODS

Human iPSC cell culture

The human induced pluripotent stem cells used are the WTC11 line, stably expressing a doxycycline-inducible hNIL construct and CRISPR/cas9. Briefly, iPSCs were seeded on tissue culture dishes coated with 120-180 µg/ml Geltrex (Thermo Fisher). Cells were maintained in iPSC medium containing Essential 8 Flex Medium (E8F, Thermo Fisher), E8 Flex supplement (Thermo Fisher), and 100 U/ml Pen/Strep and maintained in a 37 ºC, 5% CO_2 incubator. Medium change was performed every 1-2 days. Passage of cells were performed with Stem Pro Accutase (Thermo Fisher) for 1-2 min at 37 ºC. Accutase was removed by centrifugation at 300 g for 5 min, and the cells were reseeded in iPS cell media supplemented with 10 µM ROCK inhibitor (Y-27632, Selleckchem) to facilitate survival. ROCK inhibitor was removed after 24 h.

i^3 LMN differentiation from human iPS cells

Differentiation of human iPS cells was performed as previously reported Briefly, iPS cells induction was achieved using induction medium containing DMEM/F12, GlutaMAX supplement medium (Thermo Fisher), MEM non-essential amino acids (Thermo Fisher), N2 supplement (Thermo Fisher), 0.2 mM compound E, 2 µg/ml doxycycline, Pen/Strep and 10 µM ROCK inhibitor (Y-27632, Selleckchem). After induction for 48 h, differentiated motor neurons were dissociated from plates into single cells by Accutase and reseeded on poly-D-lysine (PDL)/laminin-coated tissue culture dishes or microfluidic devices in induction medium supplemented with 1 µg/ml laminin and 10 µM ROCK inhibitor. After 24 h, induction medium was replaced by motor neuron medium containing Neurobasal (Thermo Fisher), B27 Plus supplement (Thermo Fisher), N2 supplement, Culture One supplement (Thermo Fisher), 1 µg/ml laminin, 2 µg/ml doxycycline, and Pen/Strep. Medium change was performed every 1-3 days.

RNA extraction and RT-qPCR

i^3 LMNs, untreated or treated with BDNF alone or together with either ACTD or CHX, were washed with PBS before RNA was extracted using the Qiagen RNeasy isolation and purification kit following the manufacturer's protocol. RNA concentration was measured with Nanodrop, and 500 ng of RNA were used for Reverse Transcription, performed using the RevertAid cDNA synthesis kit (Thermo) following the manufacturer's protocol. Transcript levels were measured by qPCR (QuantStudio 5 Real-Time PCR system, Applied Biosystems), using delta-delta-CT method with *GAPDH* as the housekeeping gene. Primer sequences were the following: *GAPDH* forward 5′-CACCAGGGCTGCTTTTAACT-3′, *GAPDH*

reverse 5′-GACAAGCTTCCCGTTCTCAG-3′, *FOS* forward 5'-GCTTCAACGCAGACTACGAG-3', *FOS* reverse 5'-AGTGACCGTGGGAATGAAGT-3'.

Western blot analyses

Samples for western blot were denatured in lithium dodecyl sulfate (LDS, pH 8.4, NuPAGE) containing 100 mM dithiothreitol (DTT, sigma) by boiling at 99 ºC for 10 min. The denatured samples were separated on 4-12% Bis-Tris Midi gels (NuPAGE) according to the manufacturer's protocol. The separated proteins were transferred to polyvinyl difluoride (PVDF) membranes and immunoblotted using antibodies (1:1000 or 1:500 in blocking buffer; 1X PBS in 3% milk or BSA) specified in the STAR RESOURCE TABLE.

Immunofluorescence

Cells were fixed with 4% paraformaldehyde (PFA) in phosphate-buffered saline (PBS) at RT for 10 min. The fixed cells were washed with PBS three times. For permeabilization and blocking, cells were incubated with 0.1% saponin, 3% bovine serum albumin (BSA) in PBS at room temperature for 1h. The permeabilized cells were then incubated with 0.05% saponin, 3% BSA in PBS supplemented with antibodies specified in the STAR RESOURCE TABLE overnight at 4 ºC. Then, cells were washed with PBS 3 times before incubation with AlexaFluor-conjugated secondary antibody (Thermo Fisher) at RT for 1h. Cells were then washed with PBS again 5 times before confocal imaging. Images were captured using an inverted Zeiss LSM 980 microscope using a 63x oil-immersed objective.

Fabrication of tripartite microfluidic devices

We fabricated the three-compartment microfluidic devices made of polydimethylsiloxane (PDMS) with 500 µm long microgrooves, and then attached to PDL-coated Willco glass dishes and further coated with 50 µg/ml laminin and 0.8% embryonic stem (ES) BSA in DMEM/F12 medium. Prior to seeding, the chambers were washed once with Neurobasal medium. Cells were seeded into the middle 'somatic' compartment with induction media for 24h and then replaced with motor neuron media. Motor neuron media is replaced every day until DIV 10-14 prior to axotomy or live axonal transport experiments.

Manufacturing of the SOL3D open axonal platforms.

A two-part system was used for axonal isolation from cell bodies without physical barrier, consisting of microgrooves and a plating device [30]. The first part was a PDMS-based micro groove substrate (10um x10um width/height; Sylgard 184, Dow Corning). The micropatterns were created on a silicon wafer coated with SU-8 2007 (MicroChem) at 1500 rpm for 40 s using a spin coater (Polos) and then prebaked at 95 °C for 2 min. A photomask with 10 um wide stripes, interrupted every 1 cm or 5 mm for 250 um, was placed on the prebaked surface (KUB3 mask aligner) and UV exposed. The wafer was post-baked at 95 °C for 3 min, and the residual SU8 was washed off using Su8-developing liquid (MicroChem). A tissue culture friendly material was used on the above prepared master to create replicas of the microgrooves. We used a silicone elastomer PDMS. The base silicon monomer was mixed 1:10 weight/weight ratio with curing agent, mixed well and degassed. The substrate was spun on a spin coater using the above manufactured silicon master at 300 rpm. The substrate was cured to a polymer on a hotplate at 100°C for 5 min. Afterwards, the material was peeled off and cut into the desired size. Before using the substrate for tissue culture purposes, the surface was first treated with oxygen plasma (90 s, 100%, 7 sccm; Henniker Plasma), and then coated with 0.01% PDL (Gibco) for 15 min, and laminin (Sigma Aldrich). The prepared substrates were used up to 1 week after manufacturing. The plating device was manufactured using 3D vat polymerised printed molds[30] Molds were printed at 50 um z-resolution on a Phrozen Mini 4k using 4k-Aqua Grey resin (Phrozen). Afterwards, the molds were washed and

sonicated in isopropanol and then UV cured (Wash & cure, Anycubic) for 1h. To allow PDMS casting on the mold, a layer of enamel paint (Plastikote) mixed 70:30 with water was applied using an airbrush system (Timbertech). As described above, PDMS was mixed and poured into the molds. The mold was clamped in between two glass slides and cured at 75°C for 20 min.

Cell culture on the SOL3D open axonal platform.

On the day of cell seeding, plating devices were exposed to oxygen plasma (30 s, 100%, 7 sccm) (Henniker Plasma). Laminin was removed from the microgrooves and they were washed 3 times with 1x PBS, and afterwards completely dried. Plating devices were placed on the dried microgrooves. hNIL-neurons frozen at day3 of the induction protocol were defrosted, counted and seeded into the pockets of the plating device using induction medium with 1:10 Matrigel (Corning, Growth-factor reduced). Each plating device contains 6 pockets, and each pocket was filled with 300.000 cells. The cells were allowed to settle for 2h in a humidified incubator. Afterwards, cells that did not settled were washed off using 1x PBS. Then the whole well was filled with induction medium (without Matrigel) and incubated overnight. On the next day, plating devices were removed with forceps and the induction medium was aspirated. Then the whole well was filled with 1:100 Matrigel to supplement any damaged matrix during the seeding process and incubated for 2h. After aspiration of Matrigel, the well was filled with motor neuron medium. Cells were then cultured on the microgrooves until DIV 7-10 before isolation. Medium was changed every other day. For isolation of the axonal and soma components from the system, a surgical blade was used to cut through the PDMS at a distance manually adjusted (around 200 um from the soma). The two parts, soma and axon fraction, were transferred to an Eppendorf tube and put on dry ice for further isolation.

Axotomy and axonal regeneration of human motor neuron

Differentiated i^3 LMNs seeded in three-compartment MFCs were subjected to axotomy experiment at DIV12 post-differentiation. Axons were severed by strong aspiration from the axonal compartments. Starvation media was added to axonal compartments to allow repeats of axotomy until no axons could be visualized under light microscope. MN media or starvation media with drugs indicated in figure legends were added to the axonal compartment to allow axonal regrowth. After 24-48h, the level of axonal regrowth was analyzed by immunofluorescence using beta-3 tubulin to visualize axons, and acquiring images using a Zeiss LSM 980 confocal microscope, with a 20X objective. For each condition, at least 5 images from the axonal compartment were acquired. Regions with the most axonal regrowth for each condition were chosen for acquisition. For analysis, five axonal confocal images for each condition were processed using ImageJ. The images were binarized and then a standardized region-of-interest over the axons was drawn, excluding axonal debris near the microgroove openings. The total area of axons within the binarized region of interest was calculated using ImageJ. The five images per condition were averaged to represent the total area of axonal regrowth.

Intramuscular injections and in vivo live imaging of signaling endosome transport

C57BL/6J mice received unilateral injections of a muscle-specific BDNF expressing adeno-associated virus (1.4×10^{11} vector genomes of AAV8-MHCK7-BDNF) at postnatal day 22 (P22) to P23, into the tibialis anterior muscle, prior to *in vivo* imaging of signaling endosome transport at P51-P52, as performed previously [73,95]. Briefly, Refamitinib (50 nM) or DMSO vehicle control were mixed and co-injected with H_CT-555 into the AAV-treated tibialis anterior muscle, prior to intravital imaging in the intact sciatic nerve, which was performed 4-8 h later in an inverted Zeiss LSM 980 confocal microscope using a 63x(?)X oil-immersed objective at 37 °C. For signaling endosome imaging and tracking, we selected endosomes that can be tracked for ≥5 consecutive frames for analysis. 15 endosomes were tracked per axon (N= 5 animals per condition). Individual endosome speeds were averaged per animal.

Confocal live imaging was performed within 45 minutes after nerve exposure. We placed a higher preference for endosome tracking in larger caliber axons to increase the likelihood that they are motor, rather than sensory neurons, as per .

In vitro live imaging of signaling endosome transport

Differentiated i^3 LMNs were seeded into PDL and laminin coated tripartite MFCs in induction media. After 24 hrs, media was changed to motor neuron media and neurons were maintained up to DIV 9-12. 30 nM AlexaFluor555-labeled H_CT was added to the axonal compartment for 1h in growth factor/neurotrophin-free starvation media. HcT-containing media was then replaced with starvation media. BDNF (50 ng/mL) in starvation was added prior to confocal imaging. For conditions with inhibitors, 20 µM of U1206 or 0.1 µM ipatasertib was added along with the HcT. Control and treatment groups were kept on the same MFC (left and right axonal compartment). Live imaging was performed on the microgrooves to image HcT-labeled signaling endosomes located specifically in axons using an inverted Zeiss LSM 980 confocal microscope using a 40X oil-immersed objective at 37 °C. Videos were taken at 0.621 frame per second for >2.5 min using a resolution of 1024 × 1024 pixels. 3-7 kymographs were analyzed per condition with Kymoanalyzer[70] plugin. For *in vitro* endosome transport analysis in primary motor neurons, the protocol was followed as described in [96] with the same BDNF treatment strategies above, and data were analyzed using the Kymoanalyzer[70] plugin.

Kymoanalyzer analysis of signaling endosome axonal transport in i^3 LMNS

Videos of HcT-labeled signaling endosomes captured in axons of i^3 LMNs cultured in MFCs were converted into kymographs using the Kymoanalyzer[70] plugin. At least 3 kymographs were analyzed per condition. Default settings of Kymoanalyzer version were maintained during analysis. Assignment of individual signaling endosomes was performed by manual tracking of the kymographs. All motile signaling endosomes are manually tracked on the kymograph, while endosomes that are non-motile were excluded. Once the data from kymographs was pooled, average retrograde segmental velocities were used to analyze endosome retrograde velocities, whereby a combined segment is defined as an uninterrupted period of movement (anterograde or retrograde) within a tracked particle. A combined segment is framed by a pause or a reversal in direction. Pausing is defined as a segment with a segmental velocity of less than or equal to .1 µm/s.

Analysis of axonal tubulin modifications

Differentiated i^3 LMNs were seeded onto tripartite MFCs in induction media, and maintained in motor neuron media until DIV12. Plates were then treated with BDNF, U1206, and ipatasertib as described above. Cells were then washed with PBS and then simultaneously extracted and fixed with a solution containing PHEM (60 mM PIPES-NaOH, 25 mM HEPES-NaOH, 10 mM EGTA and 2 mM MgCl2, pH 6.9), 4% paraformaldehyde, 0.15% glutaraldehyde and 0.2% Triton X-100 for 15 min. Cells were then washed with PBS three times, permeabilized with 0.2% Triton X-100 in PBS for 5 min, washed again three times with PBS and blocked in 5% BSA in PBS for 1 h at room temperature. Primary anti-tyrosinated tubulin and anti-acetylated tubulin were incubated overnight at 4 ºC. Next day, cells were washed three times with PBS, incubated with AlexaFluor-conjugated secondary antibodies for 1 h at room temperature, washed again three times and mounted using Fluoromount-G (Thermo Fisher).

LC-MS/MS analysis

Cell lysates were digested using the S-trap (ProtiFi) protocol according to the manufacturer's instructions. Briefly, proteins were reduced using TCEP followed by alkylation using Iodoacetamide. Samples were acidified prior to transfer to the S-trap micro. Proteins were digested in the trap using a Trypsin/Lys-C

mix. Peptides were cleaned using Sep-Pak C18 minicolumns using the manufacturer's instructions. Cleaned peptide samples were then enriched for phospho-peptides using Titansphere TiO2 5um (GL Sciences) beads. Resultant phosphopeptides were then TMT labeled and a pool of 5% of each TMT labeled phosphopeptide sample was created and analyzed via MS to balance the input amounts for each sample. A pool of equal amounts of each labeled phosphopeptide sample was created and fractionated using a Vanquish HPLC at high pH into 48 fractions. These fractions were dried down and resuspended in 0.1% Formic acid prior to MS analysis. Fractionated phosphopeptide samples were analyzed on a Orbitrap Fusion Lumos Tribrid mass spectrometer interfaced with a 3000 RSLC nano liquid chromatography system. Roughly 1 ug of each sample were loaded onto a 2 cm trapping column (PepMap C18 100A – 300 mm. Part number: 160454. Thermo Fisher Scientific) at 5 ml/min flow rate using a loading pump and analyzed on a 50 cm analytical column (EASY-Spray column, 50 cm 75 mm ID, Part number: ES803) at 300 nl/min flow rate, that is interfaced to the mass spectrometer using Easy nLC source and electro sprayed directly into the mass spectrometer.

A linear gradient between solvent A consisting of 0.1% Formic acid (Fisher) in water (Fischer) and solvent B consisting of 0.1% Formic Acid in 99.9% Acetonitrile (Fisher). Firstly a gradient of 3% to 30% of solvent-B was used at a 300 nl/min flow rate for 105 min and 30% to 40% solvent-B for 15 min and 35% to 99% solvent-B for 5 min, which was maintained at 90% B for 10 min and washed the column at 3% solvent-B for another 10 min comprising a total of 140 min run with a 120 min gradient in a data dependent acquisition (DDA) mode. Higher energy collision induced dissociation (HCD) was used for fragmentation of peptides.

Mass spectrometry data analysis and bioinformatics analysis

Resultant MS data files were searched using MaxQuant (ver. 2.2.0) against a human database (Uniprot SwissProt database dated February 2022). The search was performed using the library-free mode using the default settings. The produced matrix of phosphopeptide abundances was processed using R (ver. 4.1.3) to normalize the data. Missing values were imputed using the Mice R package.

Statistical analysis for kinase prediction

Downstream analysis of mass-spectrometry data was performed using the R statistical software[97] The Limma R[98] package was utilized to identify differentially regulated phosphosites from normalized data. For the prediction of activated kinases, the seven amino acids flaking each detected phosphosite as well as the log2fold change and p-value determined by Limma for each site were written to a text file and uploaded to the PhosphoSitePlus[65] for kinase prediction. Volcano plots of the putative kinase activities were then generated in R using ggplot2[99] software.

Total RNA differential gene expression

Samples were aligned to the Genome Reference Consortium Human Build 38 (GRCh38) genome using hierarchical indexing for spliced alignment of transcripts - 3 nucleotides (HISAT-3N) with gene models from GENCODE v34[100,101]. Gene expression was quantified using FeatureCounts using gene models from GENCODE v34[102] For the differential expression analysis of the total RNA, all samples were run using the standard DESeq2[103] workflow in R. An adjusted p-value < 0.1 and an absolute log2Fold cutoff of 0.75 was used to determine up and downregulated genes on the total RNA level. For differential expression of the previously published RNA-seq[52] dataset, consisting of 2 hours BDNF treated H9 human embryonic stem cell-derived GABAergic inhibitory neurons, we downloaded the count and metadata matrices provided on ArrayExpress (accession no. E-MTAB-6975) and input into the standard differential expression workflow. For the gene-set enrichment analysis on the various axonal injury gene sets for

input, to account for variance, we used 'apeglm' to shrink log2Fold changes prior to the gene-set enrichment analysis.

New-to-Total RNA labeling analyses

Globally refined analysis of newly transcribed RNA and decay rates using SLAM-seq (GRAND-SLAM) was used to compute the proportion and corresponding posterior distribution of new and old RNA for each gene[32]. To test the difference in the fraction of newly transcribed RNA in BDNF and control conditions, we used a Monte-Carlo sampling model. For each gene, we first selected samples where the range of the upper and lower estimate of the newly transcribed ratio was less than 20%. If a gene did not have at least 2 of 3 samples passing this threshold, we did not assess whether the gene was differentially transcribed. Next, we generated a condition probability density for the newly transcribed ratio, by generating a beta distribution from all passing samples per condition and inversing weighting each sample by its variance. Then we sampled 1 million times from each condition-specific beta distribution and compared whether the sample was greater in BDNF versus control. Genes were categorized by comparing the fraction of the 1 million samples from each beta distribution where the estimate of new RNA in BDNF condition was higher than the estimate sampled from the control. If 90% of the sampled new RNA estimates was higher in the BDNF compared to Control, then a gene was categorized as 'bdnf_higher_new_rna', if less than 10% of samples was higher in BDNF, then a gene was categorized as 'bdnf_lower_new_rna', if the BDNF estimate was higher in 40% to 60% of the sampled new RNA estimates, the gene was categorized as 'bdnf_equals_control'.

Total gene expression clustering

Genes were hierarchically clustered by the total RNA log2Fold change across time points using 'ward.D2' method from the R stats package, and the optimal number of clusters was chosen based on a visual assessment of the cluster plot. Specifically, the plot was examined to identify the number of clusters that demonstrated the highest level of cohesion among members while maintaining a distinct separation from the other clusters. Genes which were never called as differentially expressed at any of the three timepoints and with a baseMean < 15 were removed prior to clustering. Fig. 2D shows individual gene expression as red lines, mean expression of cluster as dark blue lines, and twice width cluster standard deviation as light blue boundaries.

Transcription Factor Enrichment Analysis

Gene regulatory networks (GRN) from DoRothEA TF database[34] were first filtered to include only TF-target interactions with confidence levels A. These are the TF-target interactions with the highest level of confidence with multiple lines of evidence supporting the directional interaction, including ChIP-seq, TF binding motif on promoter, manual curation by experts in reviews, or supported in at least two curated resources. We also filtered for GRN with a minimum set size of 5 genes. DoRothEA reports both positive and negative regulatory targets and these GRN were kept as separate gene sets. In order to infer the activity of the TFs, we performed gene-set enrichment on the TF GRNs, and to control for gene expression significance, we used as input to the GRN all genes ranked according to their p-log10 transformed pvalue signed by the direction of change. GSEA was performed using the 'fgsea'[104] package in R. Full analysis available in Table S3. Significant GSEA was called with an adjusted p-value < 0.05.

Gene-ontology enrichment analyses

All gene-ontology enrichment was performed in R using the clusterProfiler[105] package. In the GO analysis combining total and NTR information, we did not include the GO genes which were either "not significant" on total RNA or where we could not accurately assess differential NTR based on the criteria

laid out in the methods section on NTR labeling. In order to ensure that enriched GO terms would pick up pathways specific to the effects of BDNF treatment and not terms related to tissue-specific expression, only genes which were detected by RNA-seq in the i^3 LMNs were used as the background gene set. Full GO term analyses are available in Table S3.

Gene set enrichment of neuronal regeneration datasets

We identified three gene sets associated with neuronal regeneration. From the Jacobi 2022[16] paper, we used the 306 genes used to create a 'composite rag score' which were selectively expressed in regenerating retinal ganglion found in Table S4 of the paper. From the Chandran 2016 paper, we selected genes from the 'magenta' module which were identified as being upregulated after peripheral nerve injury from Table S2 of the paper[14]. From the Renthal 2020 paper, we selected the genes which were common injury genes across neuronal subtypes in Table S4 of the paper[20]. We then performed GSEA against these gene sets using both the change in transcription rate, as measured by the log2Fold change of the NTR between BDNF and control, and the change in RNA abundance, as measured by the shrunken log2Fold change of total RNA.

Principal component analysis

For total RNA, count data for genes was obtained as described in the method section on *Total RNA differential gene expression.* For labeled RNA, we used the output of GRAND-SLAM which reports the number of reads with at least 2 characteristic conversions as input for count data. Count data was transformed and normalized using in the same manner for total and labeled RNA. First count data was transformed and normalized with the variance-stabilizing transformation (VST) implemented in DESeq2[103]. To focus our analysis on the most informative genes, we filtered for the top 500 genes with the highest variance before performing principal component analyses (PCA). PCA and gene loading plots, which illustrate the relative contribution of each gene to a given principal component, were generated from normalized count matrices.

SLAM-seq sequencing

SLAM-sequencing was performed on i^3 LMNs following protocols adapted from Herzog et al. (2017)[28]. i^3 LMNs were treated with 100 µM 4sU (Control) + labeling medium or 100 µM 4sU + BDNF (BDNF condition) labeling medium on Day 7 for 1h, 2h, and 6h. Cells were washed with PBS and RNA was extracted using the Qiagen RNeasy isolation and purification kit. RNA concentration was measured, and after equilibrating the amount of RNA in each sample, iodoacetamide (10 mM), NaPOH4 (pH 8, 50 mM), and DMSO (50% v/v) were added to each sample and incubated at 50 C for 15 min to facilitate the thiol-alkylation of 4sU. The samples were processed on RNeasy columns to re-isolate RNA. Sequencing libraries were prepared using the KAPA HyperPrep Kit with RiboErase kit (Roche). Samples were sequenced at 2 x 100 base pairs on an Illumina NextSeq 2000 machine.

DATA AND CODE AVAILABILITY

RNA sequencing data are available through the European Nucleotide Archive (ENA) under accession PRJEB67508. The mass spectrometry proteomics data have been deposited to the ProteomeXchange Consortium via the PRIDE, partner repository with the dataset identifier PXD046127. The codes used in this study are deposited in https://github.com/aleighbrown/lmn_bdnf. No new resources were generated in this study. BioRender was used to generate illustrations within figures.

1. Cohen-Cory, S., Kidane, A.H., Shirkey, N.J., and Marshak, S. (2010). Brain-derived neurotrophic factor and the development of structural neuronal connectivity. Devel Neurobio, NA-NA.

10.1002/dneu.20774.
2. Li, L., Xiong, W.-C., and Mei, L. (2018). Neuromuscular Junction Formation, Aging, and Disorders. Annu. Rev. Physiol. *80*, 159–188. 10.1146/annurev-physiol-022516-034255.
3. Mahar, M., and Cavalli, V. (2018). Intrinsic mechanisms of neuronal axon regeneration. Nat Rev Neurosci *19*, 323–337. 10.1038/s41583-018-0001-8.
4. Zheng, B., and Tuszynski, M.H. (2023). Regulation of axonal regeneration after mammalian spinal cord injury. Nat Rev Mol Cell Biol. 10.1038/s41580-022-00562-y.
5. Sleigh, J.N., Rossor, A.M., Fellows, A.D., Tosolini, A.P., and Schiavo, G. (2019). Axonal transport and neurological disease. Nature Reviews Neurology 2019 15:12 *15*, 691–703. 10.1038/s41582-019-0257-2.
6. Boyd, J.G., and Gordon, T. (2003). Neurotrophic Factors and Their Receptors in Axonal Regeneration and Functional Recovery After Peripheral Nerve Injury. MN *27*, 277–324. 10.1385/MN:27:3:277.
7. Scott-Solomon, E., and Kuruvilla, R. (2018). Mechanisms of neurotrophin trafficking via Trk receptors. Molecular and Cellular Neuroscience *91*, 25–33. 10.1016/J.MCN.2018.03.013.
8. Chao, M.V. (2003). Neurotrophins and their receptors: A convergence point for many signalling pathways. Nat Rev Neurosci *4*, 299–309. 10.1038/nrn1078.
9. Ginty, D.D., and Segal, R.A. (2002). Retrograde neurotrophin signaling: Trk-ing along the axon. Current Opinion in Neurobiology *12*, 268–274. 10.1016/S0959-4388(02)00326-4.
10. He, Z., and Jin, Y. (2016). Intrinsic Control of Axon Regeneration. Neuron *90*, 437–451. 10.1016/j.neuron.2016.04.022.
11. Lindsay, R. (1988). Nerve growth factors (NGF, BDNF) enhance axonal regeneration but are not required for survival of adult sensory neurons. J. Neurosci. *8*, 2394–2405. 10.1523/JNEUROSCI.08-07-02394.1988.
12. Friedman, B., Kleinfeld, D., Ip, N., Verge, V., Moulton, R., Boland, P., Zlotchenko, E., Lindsay, R., and Liu, L. (1995). BDNF and NT-4/5 exert neurotrophic influences on injured adult spinal motor neurons. J. Neurosci. *15*, 1044–1056. 10.1523/JNEUROSCI.15-02-01044.1995.
13. Geremia, N.M., Pettersson, L.M.E., Hasmatali, J.C., Hryciw, T., Danielsen, N., Schreyer, D.J., and Verge, V.M.K. (2010). Endogenous BDNF regulates induction of intrinsic neuronal growth programs in injured sensory neurons. Experimental Neurology *223*, 128–142. 10.1016/j.expneurol.2009.07.022.
14. Chandran, V., Coppola, G., Nawabi, H., Omura, T., Versano, R., Huebner, E.A., Zhang, A., Costigan, M., Yekkirala, A., Barrett, L., et al. (2016). A Systems-Level Analysis of the Peripheral Nerve Intrinsic Axonal Growth Program. Neuron *89*, 956–970. 10.1016/j.neuron.2016.01.034.
15. Moore, D.L., and Goldberg, J.L. (2011). Multiple transcription factor families regulate axon growth and regeneration. Devel Neurobio *71*, 1186–1211. 10.1002/dneu.20934.
16. Jacobi, A., Tran, N.M., Yan, W., Benhar, I., Tian, F., Schaffer, R., He, Z., and Sanes, J.R. (2022). Overlapping transcriptional programs promote survival and axonal regeneration of injured retinal ganglion cells. Neuron *110*, 2625-2645.e7. 10.1016/j.neuron.2022.06.002.
17. Tian, F., Cheng, Y., Zhou, S., Wang, Q., Monavarfeshani, A., Gao, K., Jiang, W., Kawaguchi, R., Wang, Q., Tang, M., et al. (2022). Core transcription programs controlling injury-induced neurodegeneration of retinal ganglion cells. Neuron *110*, 2607-2624.e8. 10.1016/j.neuron.2022.06.003.
18. Qian, C., and Zhou, F.-Q. (2020). Updates and challenges of axon regeneration in the mammalian central nervous system. Journal of Molecular Cell Biology *12*, 798–806. 10.1093/jmcb/mjaa026.
19. Poplawski, G.H.D., Kawaguchi, R., Van Niekerk, E., Lu, P., Mehta, N., Canete, P., Lie, R., Dragatsis, I., Meves, J.M., Zheng, B., et al. (2020). Injured adult neurons regress to an embryonic transcriptional growth state. Nature *581*, 77–82. 10.1038/s41586-020-2200-5.
20. Renthal, W., Tochitsky, I., Yang, L., Cheng, Y.-C., Li, E., Kawaguchi, R., Geschwind, D.H., and Woolf, C.J. (2020). Transcriptional Reprogramming of Distinct Peripheral Sensory Neuron Subtypes after Axonal Injury. Neuron *108*, 128-144.e9. 10.1016/j.neuron.2020.07.026.
21. Moya-Alvarado, G., Tiburcio-Felix, R., Ibáñez, M.R., Aguirre-Soto, A.A., Guerra, M.V., Wu, C.,

Mobley, W.C., Perlson, E., and Bronfman, F.C. (2023). BDNF/TrkB signaling endosomes in axons coordinate CREB/mTOR activation and protein synthesis in the cell body to induce dendritic growth in cortical neurons. eLife *12*, e77455. 10.7554/eLife.77455.

22. Gonzalez, A., Moya-Alvarado, G., Gonzalez-Billaut, C., and Bronfman, F.C. (2016). Cellular and molecular mechanisms regulating neuronal growth by brain-derived neurotrophic factor: Neuronal Growth by Brain-Derived Neurotrophic Factor. Cytoskeleton *73*, 612–628. 10.1002/cm.21312.
23. Blanquie, O., and Bradke, F. (2018). Cytoskeleton dynamics in axon regeneration. Current Opinion in Neurobiology *51*, 60–69. 10.1016/j.conb.2018.02.024.
24. Janke, C., and Magiera, M.M. (2020). The tubulin code and its role in controlling microtubule properties and functions. Nat Rev Mol Cell Biol *21*, 307–326. 10.1038/s41580-020-0214-3.
25. Atkins, M., Nicol, X., and Fassier, C. (2023). Microtubule remodelling as a driving force of axon guidance and pruning. Seminars in Cell & Developmental Biology *140*, 35–53. 10.1016/j.semcdb.2022.05.030.
26. Bodakuntla, S., Jijumon, A.S., Villablanca, C., Gonzalez-Billault, C., and Janke, C. (2019). Microtubule-Associated Proteins: Structuring the Cytoskeleton. Trends in Cell Biology *29*, 804–819. 10.1016/j.tcb.2019.07.004.
27. Ramkumar, A., Jong, B.Y., and Ori-McKenney, K.M. (2018). ReMAPping the microtubule landscape: How phosphorylation dictates the activities of microtubule-associated proteins: Phosphorylation of Microtubule-Associated Proteins. Dev. Dyn. *247*, 138–155. 10.1002/dvdy.24599.
28. Herzog, V.A., Reichholf, B., Neumann, T., Rescheneder, P., Bhat, P., Burkard, T.R., Wlotzka, W., Von Haeseler, A., Zuber, J., and Ameres, S.L. (2017). Thiol-linked alkylation of RNA to assess expression dynamics. Nat Methods *14*, 1198–1204. 10.1038/nmeth.4435.
29. Fernandopulle, M.S., Prestil, R., Grunseich, C., Wang, C., Gan, L., and Ward, M.E. (2018). Transcription Factor-Mediated Differentiation of Human iPSCs into Neurons: Rapid differentiation of iPSCs into neurons. Current Protocols in Cell Biology *79*, e51. 10.1002/cpcb.51.
30. Hagemann, C., Bailey, M.C.D., Lionello, V.M., Khokhar, N., Suklai, P., Moreno-Gonzalez, C., O'Toole, K., Konstantinou, G., Joshi, S., Giagnorio, E., et al. (2022). SOLID: Soft-lithography on SLA 3D printed moulds for fast, versatile, and accessible high-resolution fabrication of customised multiscale cell culture devices with complex designs (Bioengineering) 10.1101/2022.02.22.481424.
31. Hagemann, C., Moreno Gonzalez, C., Guetta, L., Tyzack, G., Chiappini, C., Legati, A., Patani, R., and Serio, A. (2022). Axonal Length Determines Distinct Homeostatic Phenotypes in Human iPSC Derived Motor Neurons on a Bioengineered Platform. Adv Healthcare Materials *11*, 2101817. 10.1002/adhm.202101817.
32. Jürges, C., Dölken, L., and Erhard, F. (2018). Dissecting newly transcribed and old RNA using GRAND-SLAM. Bioinformatics *34*, i218–i226. 10.1093/bioinformatics/bty256.
33. Neumann, T., Herzog, V.A., Muhar, M., von Haeseler, A., Zuber, J., Ameres, S.L., and Rescheneder, P. (2019). Quantification of experimentally induced nucleotide conversions in high-throughput sequencing datasets. BMC Bioinformatics *20*, 1–16. 10.1186/s12859-019-2849-7.
34. Garcia-Alonso, L., Holland, C.H., Ibrahim, M.M., Turei, D., and Saez-Rodriguez, J. (2019). Benchmark and integration of resources for the estimation of human transcription factor activities. Genome Res *29*, 1363–1375. 10.1101/gr.240663.118.
35. Abe, N., and Cavalli, V. (2008). Nerve injury signaling. Current Opinion in Neurobiology *18*, 276–283. 10.1016/j.conb.2008.06.005.
36. Ben-Yaakov, K., Dagan, S.Y., Segal-Ruder, Y., Shalem, O., Vuppalanchi, D., Willis, D.E., Yudin, D., Rishal, I., Rother, F., Bader, M., et al. (2012). Axonal transcription factors signal retrogradely in lesioned peripheral nerve: Axonal transcription factors in lesioned nerve. The EMBO Journal *31*, 1350–1363. 10.1038/emboj.2011.494.
37. Di Giovanni, S., Knights, C.D., Rao, M., Yakovlev, A., Beers, J., Catania, J., Avantaggiati, M.L., and Faden, A.I. (2006). The tumor suppressor protein p53 is required for neurite outgrowth and axon regeneration. EMBO J *25*, 4084–4096. 10.1038/sj.emboj.7601292.
38. Tedeschi, A., Nguyen, T., Puttagunta, R., Gaub, P., and Di Giovanni, S. (2009). A p53-CBP/p300

transcription module is required for GAP-43 expression, axon outgrowth, and regeneration. Cell Death Differ *16*, 543–554. 10.1038/cdd.2008.175.
39. Gao, Y., Deng, K., Hou, J., Bryson, J.B., Barco, A., Nikulina, E., Spencer, T., Mellado, W., Kandel, E.R., and Filbin, M.T. (2004). Activated CREB Is Sufficient to Overcome Inhibitors in Myelin and Promote Spinal Axon Regeneration In Vivo. Neuron *44*, 609–621. 10.1016/j.neuron.2004.10.030.
40. Noro, T., Shah, S.H., Yin, Y., Kawaguchi, R., Yokota, S., Chang, K.-C., Madaan, A., Sun, C., Coppola, G., Geschwind, D., et al. (2022). Elk-1 regulates retinal ganglion cell axon regeneration after injury. Sci Rep *12*, 17446. 10.1038/s41598-022-21767-3.
41. Stern, S., Haverkamp, S., Sinske, D., Tedeschi, A., Naumann, U., Di Giovanni, S., Kochanek, S., Nordheim, A., and Knöll, B. (2013). The Transcription Factor Serum Response Factor Stimulates Axon Regeneration through Cytoplasmic Localization and Cofilin Interaction. J. Neurosci. *33*, 18836–18848. 10.1523/JNEUROSCI.3029-13.2013.
42. Gu, M., Li, X., Wu, R., Cheng, X., Zhou, S., and Gu, X. (2023). The Transcription Factor Ets1 Influences Axonal Growth via Regulation of Lcn2. Mol Neurobiol. 10.1007/s12035-023-03616-0.
43. Raivich, G., Bohatschek, M., Da Costa, C., Iwata, O., Galiano, M., Hristova, M., Nateri, A.S., Makwana, M., Riera-Sans, L., Wolfer, D.P., et al. (2004). The AP-1 Transcription Factor c-Jun Is Required for Efficient Axonal Regeneration. Neuron *43*, 57–67. 10.1016/j.neuron.2004.06.005.
44. Herdegen, T., Brecht, S., Mayer, B., Leah, J., Kummer, W., Bravo, R., and Zimmermann, M. (1993). Long-lasting expression of JUN and KROX transcription factors and nitric oxide synthase in intrinsic neurons of the rat brain following axotomy. J. Neurosci. *13*, 4130–4145. 10.1523/JNEUROSCI.13-10-04130.1993.
45. Kiryu-Seo, S., Kato, R., Ogawa, T., Nakagomi, S., Nagata, K., and Kiyama, H. (2008). Neuronal Injury-inducible Gene Is Synergistically Regulated by ATF3, c-Jun, and STAT3 through the Interaction with Sp1 in Damaged Neurons. Journal of Biological Chemistry *283*, 6988–6996. 10.1074/jbc.M707514200.
46. Seijffers, R., Mills, C.D., and Woolf, C.J. (2007). ATF3 Increases the Intrinsic Growth State of DRG Neurons to Enhance Peripheral Nerve Regeneration. J. Neurosci. *27*, 7911–7920. 10.1523/JNEUROSCI.5313-06.2007.
47. Gey, M., Wanner, R., Schilling, C., Pedro, M.T., Sinske, D., and Knöll, B. (2016). *Atf3* mutant mice show reduced axon regeneration and impaired regeneration-associated gene induction after peripheral nerve injury. Open Biol. *6*, 160091. 10.1098/rsob.160091.
48. Erhard, F., Baptista, M.A.P., Krammer, T., Hennig, T., Lange, M., Arampatzi, P., Jürges, C.S., Theis, F.J., Saliba, A.-E., and Dölken, L. (2019). scSLAM-seq reveals core features of transcription dynamics in single cells. Nature *571*, 419–423. 10.1038/s41586-019-1369-y.
49. Liu, H., Arsiè, R., Schwabe, D., Schilling, M., Minia, I., Alles, J., Boltengagen, A., Kocks, C., Falcke, M., Friedman, N., et al. (2023). SLAM-Drop-seq reveals mRNA kinetic rates throughout the cell cycle. Molecular Systems Biology *n/a*, e11427. 10.15252/msb.202211427.
50. Koley, S., Rozenbaum, M., Fainzilber, M., and Terenzio, M. (2019). Translating regeneration: Local protein synthesis in the neuronal injury response. Neuroscience Research *139*, 26–36. 10.1016/j.neures.2018.10.003.
51. Garcia, A.L., Udeh, A., Kalahasty, K., and Hackam, A.S. (2018). A growing field: The regulation of axonal regeneration by Wnt signaling. Neural Regen Res *13*, 43–52. 10.4103/1673-5374.224359.
52. Merkouris, S., Barde, Y.-A., Binley, K.E., Allen, N.D., Stepanov, A.V., Wu, N.C., Grande, G., Lin, C.-W., Li, M., Nan, X., et al. (2018). Fully human agonist antibodies to TrkB using autocrine cell-based selection from a combinatorial antibody library. Proceedings of the National Academy of Sciences *115*, E7023–E7032. 10.1073/pnas.1806660115.
53. Gonzalez-Perez, F., Udina, E., and Navarro, X. (2013). Extracellular Matrix Components in Peripheral Nerve Regeneration. In International Review of Neurobiology (Elsevier), pp. 257–275. 10.1016/B978-0-12-410499-0.00010-1.
54. Dave, P., Roth, G., Griesbach, E., Mateju, D., Hochstoeger, T., and Chao, J.A. (2023). Single-molecule imaging reveals translation-dependent destabilization of mRNAs. Molecular Cell *83*,

589-606.e6. 10.1016/j.molcel.2023.01.013.
55. Liao, L., Pilotte, J., Xu, T., Wong, C.C.L., Edelman, G.M., Vanderklish, P., and Yates, J.R. (2007). BDNF Induces Widespread Changes in Synaptic Protein Content and Up-Regulates Components of the Translation Machinery: An Analysis Using High-Throughput Proteomics. J. Proteome Res. *6*, 1059–1071. 10.1021/pr060358f.
56. Shin, J.E., Geisler, S., and DiAntonio, A. (2014). Dynamic regulation of SCG10 in regenerating axons after injury. Experimental Neurology *252*, 1–11. 10.1016/j.expneurol.2013.11.007.
57. Amen, A.M., Ruiz-Garzon, C.R., Shi, J., Subramanian, M., Pham, D.L., and Meffert, M.K. (2017). A Rapid Induction Mechanism for Lin28a in Trophic Responses. Molecular Cell *65*, 490-503.e7. 10.1016/j.molcel.2016.12.025.
58. Nathan, F.M., Ohtake, Y., Wang, S., Jiang, X., Sami, A., Guo, H., Zhou, F.-Q., and Li, S. (2020). Upregulating Lin28a Promotes Axon Regeneration in Adult Mice with Optic Nerve and Spinal Cord Injury. Molecular Therapy *28*, 1902–1917. 10.1016/j.ymthe.2020.04.010.
59. Zhang, Y., Williams, P.R., Jacobi, A., Wang, C., Goel, A., Hirano, A.A., Brecha, N.C., Kerschensteiner, D., and He, Z. (2019). Elevating Growth Factor Responsiveness and Axon Regeneration by Modulating Presynaptic Inputs. Neuron *103*, 39-51.e5. 10.1016/j.neuron.2019.04.033.
60. Bright, N.J., Carling, D., and Thornton, C. (2008). Investigating the Regulation of Brain-specific Kinases 1 and 2 by Phosphorylation. Journal of Biological Chemistry *283*, 14946–14954. 10.1074/jbc.M710381200.
61. Kishi, M., Pan, Y.A., Crump, J.G., and Sanes, J.R. (2005). Mammalian SAD Kinases Are Required for Neuronal Polarization. Science *307*, 929–932. 10.1126/science.1107403.
62. Decourt, C., Schaeffer, J., Blot, B., Paccard, A., Excoffier, B., Pende, M., Nawabi, H., and Belin, S. (2023). The RSK2-RPS6 axis promotes axonal regeneration in the peripheral and central nervous systems. PLoS Biol *21*, e3002044. 10.1371/journal.pbio.3002044.
63. Wagih, O. (2017). ggseqlogo: a versatile R package for drawing sequence logos. Bioinformatics *33*, 3645–3647. 10.1093/bioinformatics/btx469.
64. Pearce, L.R., Komander, D., and Alessi, D.R. (2010). The nuts and bolts of AGC protein kinases. Nat Rev Mol Cell Biol *11*, 9–22. 10.1038/nrm2822.
65. Johnson, J.L., Yaron, T.M., Huntsman, E.M., Kerelsky, A., Song, J., Regev, A., Lin, T.-Y., Liberatore, K., Cizin, D.M., Cohen, B.M., et al. (2023). An atlas of substrate specificities for the human serine/threonine kinome. Nature *613*, 759–766. 10.1038/s41586-022-05575-3.
66. Anjum, R., and Blenis, J. (2008). The RSK family of kinases: emerging roles in cellular signalling. Nat Rev Mol Cell Biol *9*, 747–758. 10.1038/nrm2509.
67. Mao, S., Chen, Y., Feng, W., Zhou, S., Jiang, C., Zhang, J., Liu, X., Qian, T., Liu, K., Wang, Y., et al. (2022). RSK1 promotes mammalian axon regeneration by inducing the synthesis of regeneration-related proteins. PLoS Biol *20*, e3001653. 10.1371/journal.pbio.3001653.
68. Gibbs, K.L., Kalmar, B., Rhymes, E.R., Fellows, A.D., Ahmed, M., Whiting, P., Davies, C.H., Greensmith, L., and Schiavo, G. (2018). Inhibiting p38 MAPK alpha rescues axonal retrograde transport defects in a mouse model of ALS. Cell Death Dis *9*, 596. 10.1038/s41419-018-0624-8.
69. Lalli, G., and Schiavo, G. (2002). Analysis of retrograde transport in motor neurons reveals common endocytic carriers for tetanus toxin and neurotrophin receptor p75NTR. The Journal of Cell Biology *156*, 233–240. 10.1083/jcb.200106142.
70. Neumann, S., Chassefeyre, R., Campbell, G.E., and Encalada, S.E. (2017). KymoAnalyzer: a software tool for the quantitative analysis of intracellular transport in neurons: NEUMANN ET AL . Traffic *18*, 71–88. 10.1111/tra.12456.
71. Tosolini, A.P., Sleigh, J.N., Surana, S., Rhymes, E.R., Cahalan, S.D., and Schiavo, G. (2022). BDNF-dependent modulation of axonal transport is selectively impaired in ALS. acta neuropathol commun *10*, 121. 10.1186/s40478-022-01418-4.
72. Fellows, A.D., Rhymes, E.R., Gibbs, K.L., Greensmith, L., and Schiavo, G. (2020). IGF 1R regulates retrograde axonal transport of signalling endosomes in motor neurons. EMBO Reports *21*.

10.15252/embr.201949129.
73. Sleigh, J.N., Villarroel-Campos, D., Surana, S., Wickenden, T., Tong, Y., Simkin, R.L., Vargas, J.N.S., Rhymes, E.R., Tosolini, A.P., West, S.J., et al. (2023). Boosting peripheral BDNF rescues impaired in vivo axonal transport in CMT2D mice. JCI Insight. 10.1172/jci.insight.157191.
74. Ho, T.S.-Y., Hees, J.T., Xu, Z., Kawaguchi, R., Biscola, N.P., Taub, D.G., Chen, K., Chen, X., Barrett, L.B., Cheng, L., et al. (2021). Screening for axon regeneration promoting compounds with human iPSC-derived motor neurons. Preprint at bioRxiv, 10.1101/2021.11.02.466937 10.1101/2021.11.02.466937.
75. Keefe, K., Sheikh, I., and Smith, G. (2017). Targeting Neurotrophins to Specific Populations of Neurons: NGF, BDNF, and NT-3 and Their Relevance for Treatment of Spinal Cord Injury. IJMS *18*, 548. 10.3390/ijms18030548.
76. Terenghi, G. (1999). Peripheral nerve regeneration and neurotrophic factors. J Anatomy *194*, 1–14. 10.1046/j.1469-7580.1999.19410001.x.
77. Lykissas, M., Batistatou, A., Charalabopoulos, K., and Beris, A. (2007). The Role of Neurotrophins in Axonal Growth, Guidance, and Regeneration. CNR *4*, 143–151. 10.2174/156720207780637216.
78. Patange, S., Ball, D.A., Wan, Y., Karpova, T.S., Girvan, M., Levens, D., and Larson, D.R. (2022). MYC amplifies gene expression through global changes in transcription factor dynamics. Cell Reports *38*, 110292. 10.1016/j.celrep.2021.110292.
79. Lu, B. (2003). BDNF and Activity-Dependent Synaptic Modulation: Figure 1. Learn. Mem. *10*, 86–98. 10.1101/lm.54603.
80. Conde, C., and Cáceres, A. (2009). Microtubule assembly, organization and dynamics in axons and dendrites. Nat Rev Neurosci *10*, 319–332. 10.1038/nrn2631.
81. Dogterom, M., and Koenderink, G.H. (2019). Actin–microtubule crosstalk in cell biology. Nat Rev Mol Cell Biol *20*, 38–54. 10.1038/s41580-018-0067-1.
82. Jijumon, A.S., Bodakuntla, S., Genova, M., Bangera, M., Sackett, V., Besse, L., Maksut, F., Henriot, V., Magiera, M.M., Sirajuddin, M., et al. (2022). Lysate-based pipeline to characterize microtubule-associated proteins uncovers unique microtubule behaviours. Nat Cell Biol *24*, 253–267. 10.1038/s41556-021-00825-4.
83. Agthong, S., Koonam, J., Kaewsema, A., and Chentanez, V. (2009). Inhibition of MAPK ERK impairs axonal regeneration without an effect on neuronal loss after nerve injury. Neurological Research *31*, 1068–1074. 10.1179/174313209X380883.
84. Hollis, E.R., Jamshidi, P., Löw, K., Blesch, A., and Tuszynski, M.H. (2009). Induction of corticospinal regeneration by lentiviral trkB-induced Erk activation. Proc. Natl. Acad. Sci. U.S.A. *106*, 7215–7220. 10.1073/pnas.0810624106.
85. Namikawa, K., Honma, M., Abe, K., Takeda, M., Mansur, K., Obata, T., Miwa, A., Okado, H., and Kiyama, H. (2000). Akt/Protein Kinase B Prevents Injury-Induced Motoneuron Death and Accelerates Axonal Regeneration. J. Neurosci. *20*, 2875–2886. 10.1523/JNEUROSCI.20-08-02875.2000.
86. Park, K.K., Liu, K., Hu, Y., Smith, P.D., Wang, C., Cai, B., Xu, B., Connolly, L., Kramvis, I., Sahin, M., et al. (2008). Promoting axon regeneration in the adult CNS by modulation of the PTEN/mTOR pathway. Science (New York, N.Y.) *322*, 963–966. 10.1126/science.1161566.
87. Sun, F., Park, K.K., Belin, S., Wang, D., Lu, T., Chen, G., Zhang, K., Yeung, C., Feng, G., Yankner, B.A., et al. (2011). Sustained axon regeneration induced by co-deletion of PTEN and SOCS3. Nature *480*, 372–375. 10.1038/nature10594.
88. Du, K., Zheng, S., Zhang, Q., Li, S., Gao, X., Wang, J., Jiang, L., and Liu, K. (2015). Pten Deletion Promotes Regrowth of Corticospinal Tract Axons 1 Year after Spinal Cord Injury. Journal of Neuroscience *35*, 9754–9763. 10.1523/JNEUROSCI.3637-14.2015.
89. Villarroel-Campos, D., Schiavo, G., and Lazo, O.M. (2018). The many disguises of the signalling endosome. FEBS Lett *592*, 3615–3632. 10.1002/1873-3468.13235.
90. Lazo, O.M., and Schiavo, G. (2023). Rab10 regulates the sorting of internalised TrkB for retrograde axonal transport. eLife *12*, e81532. 10.7554/eLife.81532.

91. Perlson, E., Hanz, S., Ben-Yaakov, K., Segal-Ruder, Y., Seger, R., and Fainzilber, M. (2005). Vimentin-Dependent Spatial Translocation of an Activated MAP Kinase in Injured Nerve. Neuron *45*, 715–726. 10.1016/j.neuron.2005.01.023.
92. Elena R. Rhymes, Rebecca L. Simkin, Sunaina Surana, Yao Tong, David Villarroel-Campos, Xiang-Lei Yang, Giampietro Schiavo, and James N. Sleigh (2023). Boosting BDNF in muscle rescues impaired in vivo axonal transport in a mouse model of DI-CMTC peripheral neuropathy. bioRxiv, 2023.04.09.536152. 10.1101/2023.04.09.536152.
93. Mead, R.J., Shan, N., Reiser, H.J., Marshall, F., and Shaw, P.J. (2023). Amyotrophic lateral sclerosis: a neurodegenerative disorder poised for successful therapeutic translation. Nat Rev Drug Discov *22*, 185–212. 10.1038/s41573-022-00612-2.
94. Raudvere, U., Kolberg, L., Kuzmin, I., Arak, T., Adler, P., Peterson, H., and Vilo, J. (2019). g:Profiler: a web server for functional enrichment analysis and conversions of gene lists (2019 update). Nucleic Acids Res *47*, W191–W198. 10.1093/nar/gkz369.
95. Sleigh, J.N., Tosolini, A.P., and Schiavo, G. (2020). In Vivo Imaging of Anterograde and Retrograde Axonal Transport in Rodent Peripheral Nerves. In Axon Degeneration Methods in Molecular Biology., E. Babetto, ed. (Springer US), pp. 271–292. 10.1007/978-1-0716-0585-1_20.
96. Rhymes, E.R., Tosolini, A.P., Fellows, A.D., Mahy, W., McDonald, N.Q., and Schiavo, G. (2022). Bimodal regulation of axonal transport by the GDNF-RET signalling axis in healthy and diseased motor neurons. Cell Death Dis *13*, 584. 10.1038/s41419-022-05031-0.
97. R: The R Project for Statistical Computing https://www.r-project.org/.
98. Ritchie, M.E., Phipson, B., Wu, D., Hu, Y., Law, C.W., Shi, W., and Smyth, G.K. (2015). limma powers differential expression analyses for RNA-sequencing and microarray studies. Nucleic Acids Res *43*, e47. 10.1093/nar/gkv007.
99. Wickham, H., Chang, W., Henry, L., Pedersen, T.L., Takahashi, K., Wilke, C., Woo, K., Yutani, H., Dunnington, D., Posit, et al. (2023). ggplot2: Create Elegant Data Visualisations Using the Grammar of Graphics. Version 3.4.2.
100. Frankish, A., Diekhans, M., Ferreira, A.-M., Johnson, R., Jungreis, I., Loveland, J., Mudge, J.M., Sisu, C., Wright, J., Armstrong, J., et al. (2019). GENCODE reference annotation for the human and mouse genomes. Nucleic Acids Res *47*, D766–D773. 10.1093/nar/gky955.
101. Zhang, Y., Park, C., Bennett, C., Thornton, M., and Kim, D. (2021). Rapid and accurate alignment of nucleotide conversion sequencing reads with HISAT-3N. Genome Res. *31*, 1290–1295. 10.1101/gr.275193.120.
102. Liao, Y., Smyth, G.K., and Shi, W. (2014). featureCounts: an efficient general purpose program for assigning sequence reads to genomic features. Bioinformatics *30*, 923–930. 10.1093/bioinformatics/btt656.
103. Love, M.I., Huber, W., and Anders, S. (2014). Moderated estimation of fold change and dispersion for RNA-seq data with DESeq2. Genome Biology *15*, 550. 10.1186/s13059-014-0550-8.
104. Korotkevich, G., Sukhov, V., Budin, N., Shpak, B., Artyomov, M.N., and Sergushichev, A. (2021). Fast gene set enrichment analysis. Preprint at bioRxiv, 10.1101/060012 10.1101/060012.
105. Yu, G., Wang, L.-G., Han, Y., and He, Q.-Y. (2012). clusterProfiler: an R package for comparing biological themes among gene clusters. OMICS *16*, 284–287. 10.1089/omi.2011.0118.

Fig. 1. BDNF signaling in human iPSC-derived motor neurons i³ LMNs

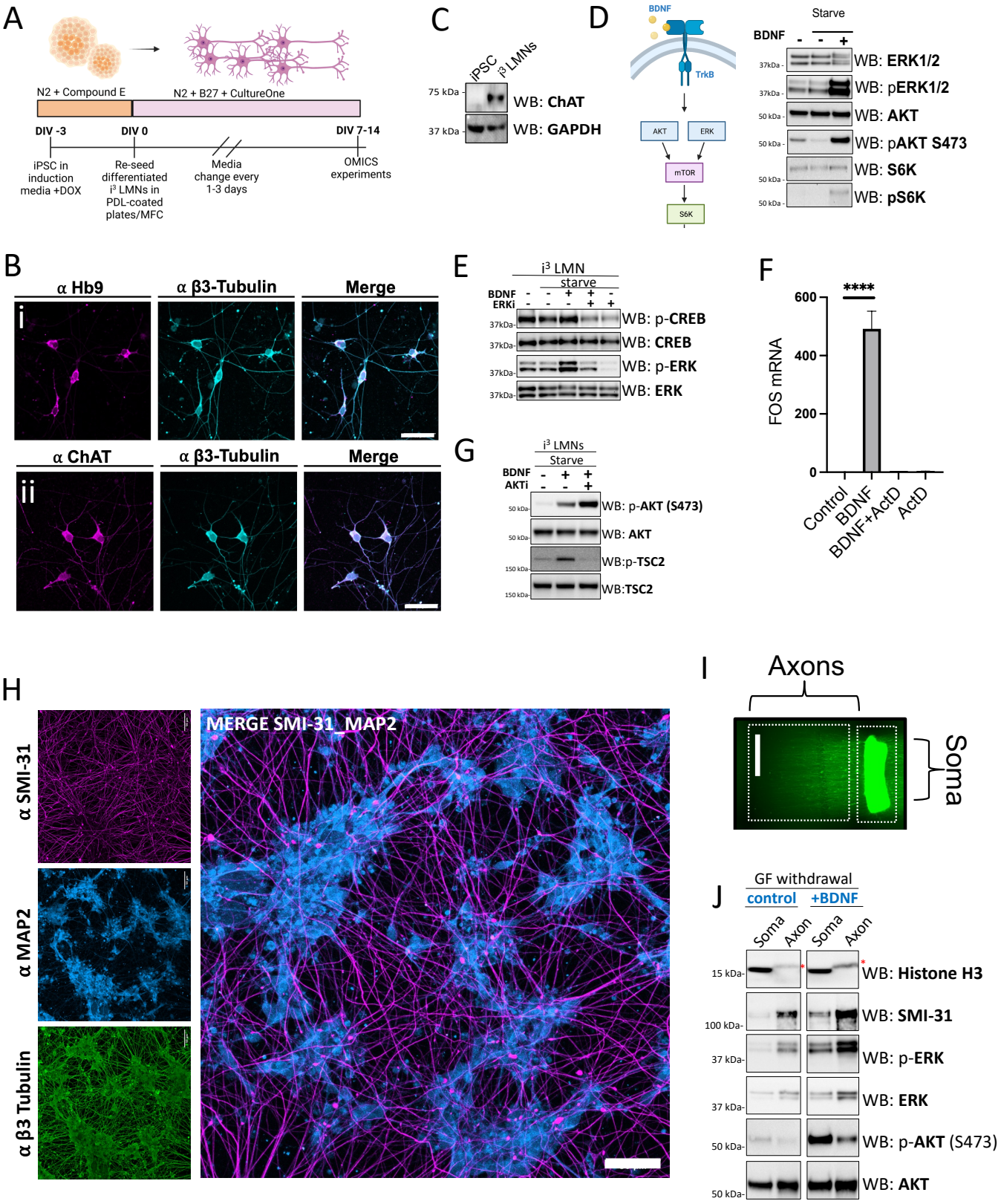

Fig. S1. BDNF response and differentiation of iPSC-derived lower motor neurons

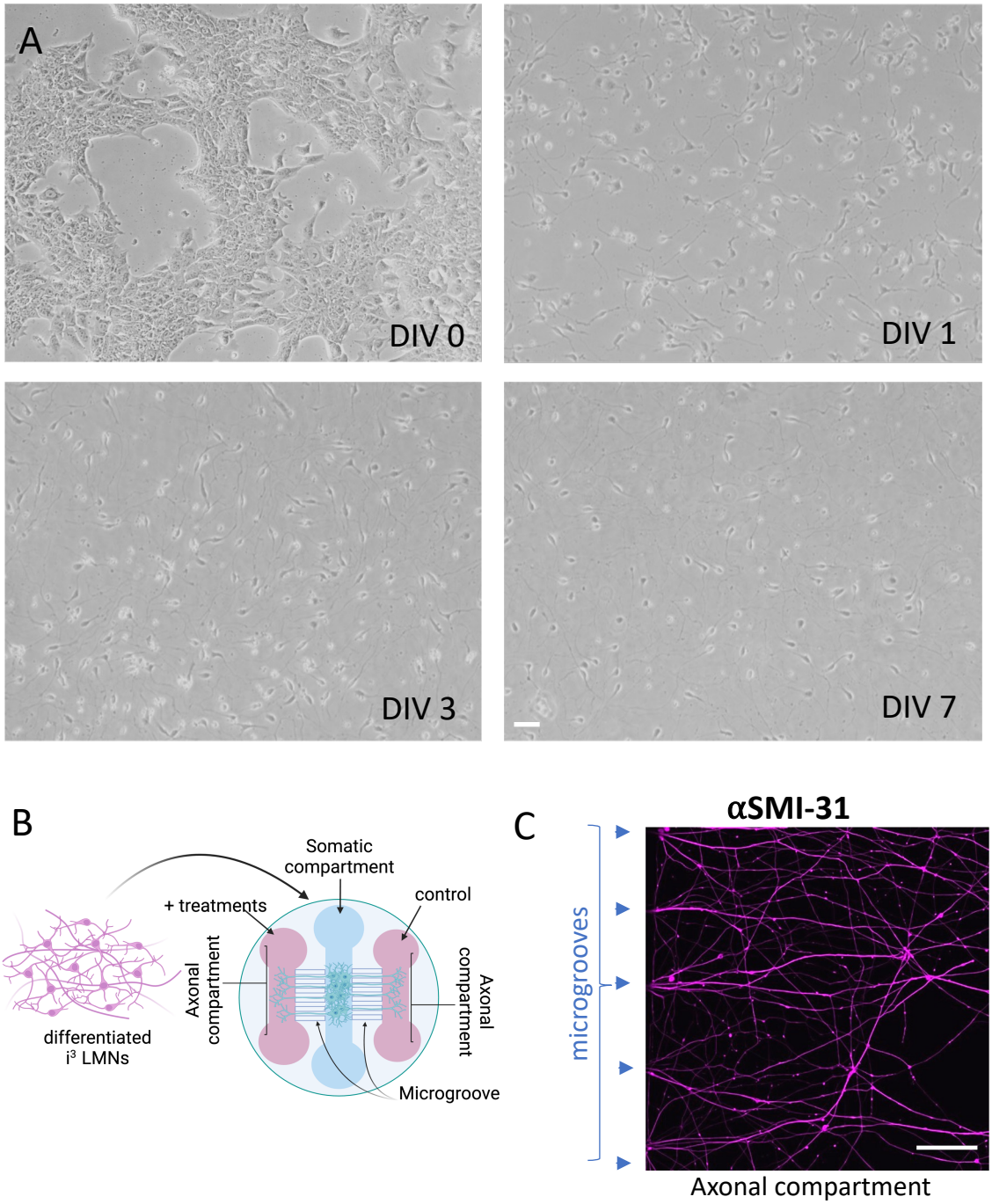

Fig. 2. Profiling the temporal dynamics of BDNF-dependent transcription in human motor neuron

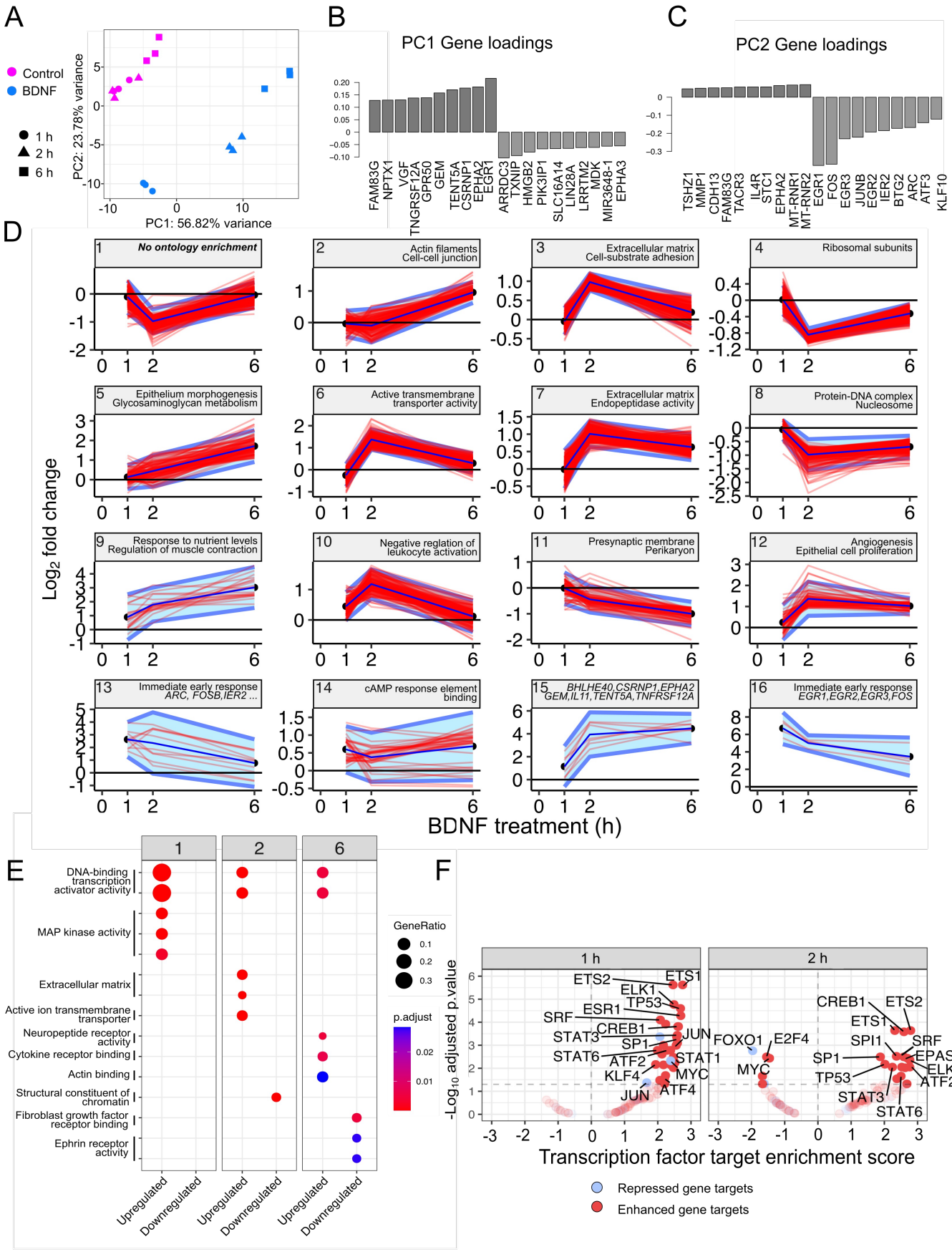

Fig. S2. BDNF-driven gene expression in human motor neurons

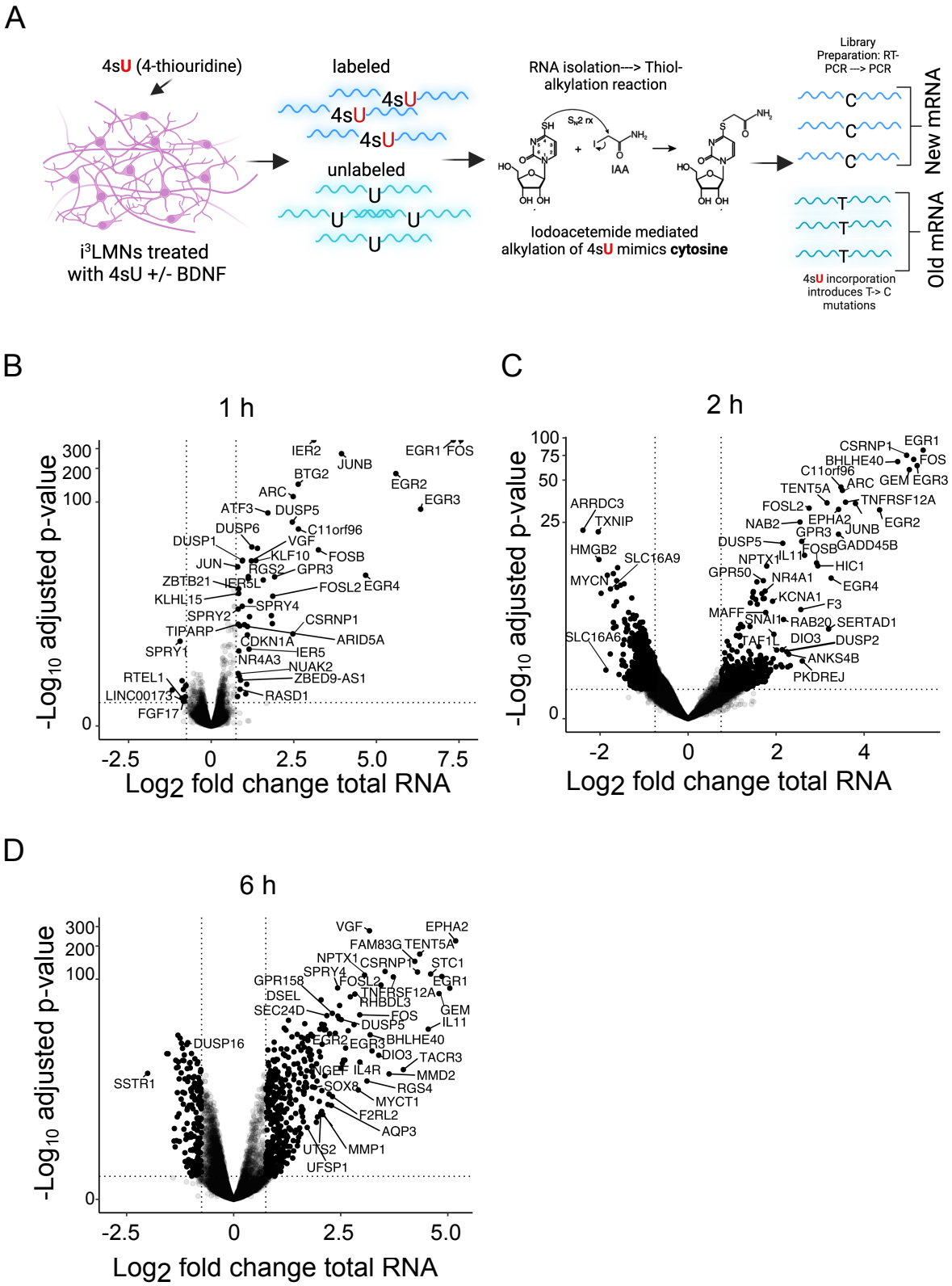

Fig. 3. SLAM-sequencing uncovers BDNF-driven RNA dynamics in human motor neurons

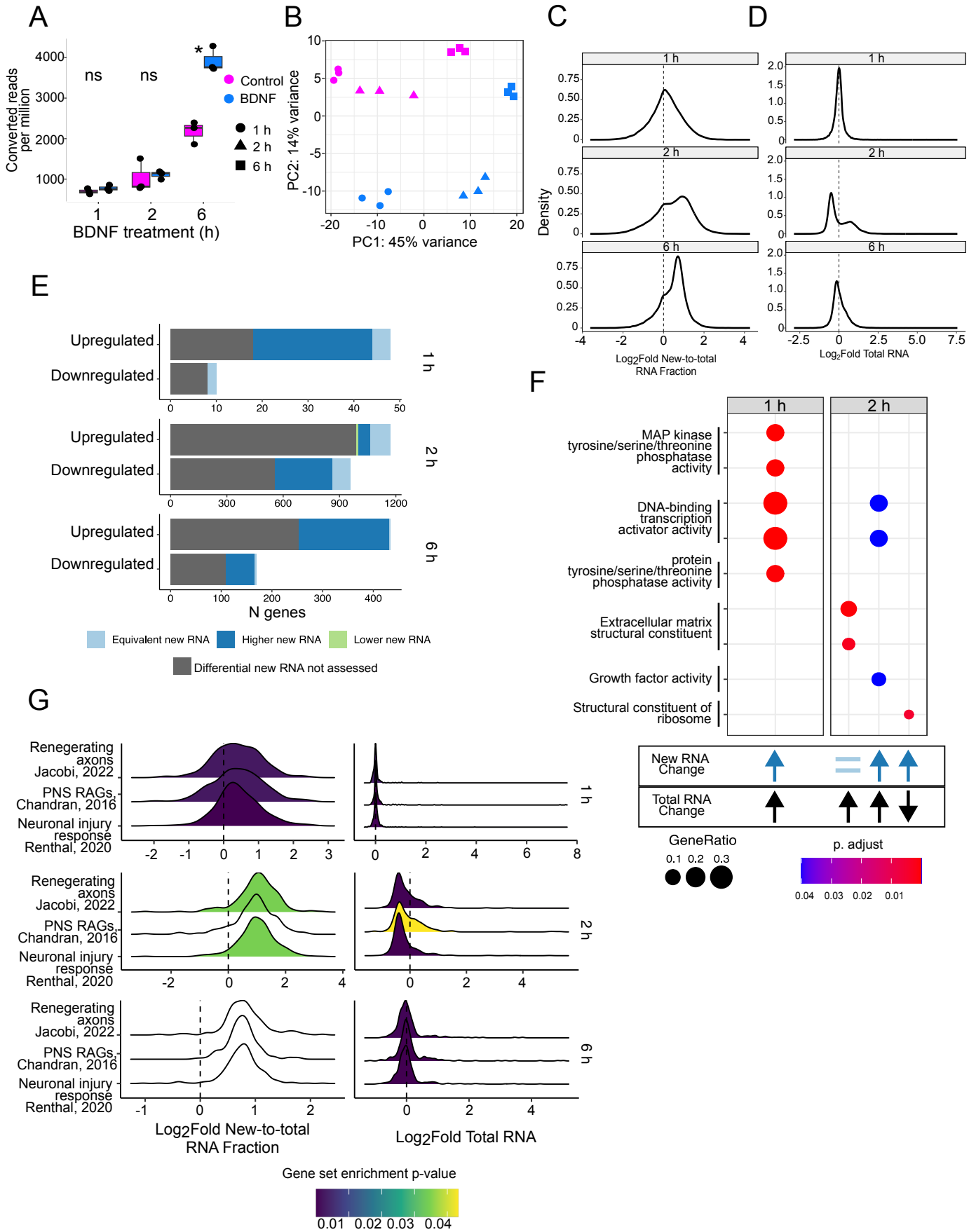

Figure S3. SLAM-sequencing reveals differential effects of BDNF on total and new RNA

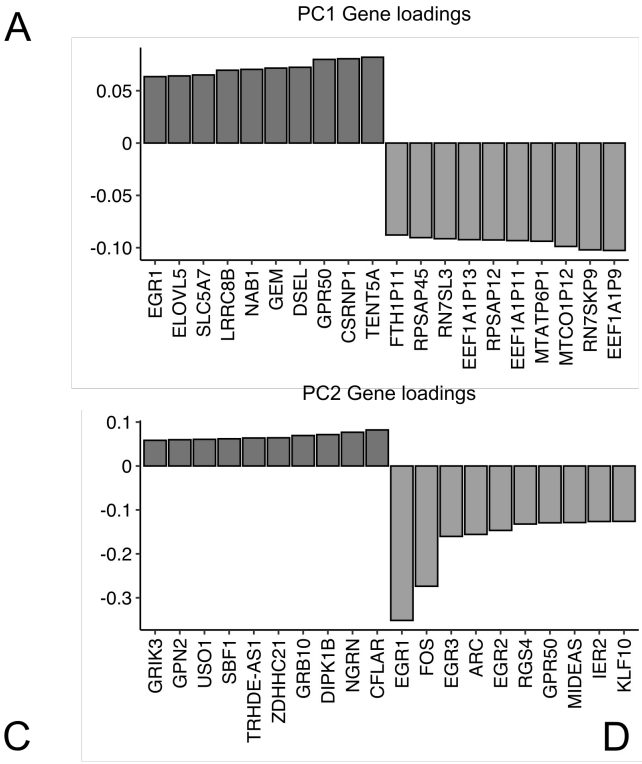

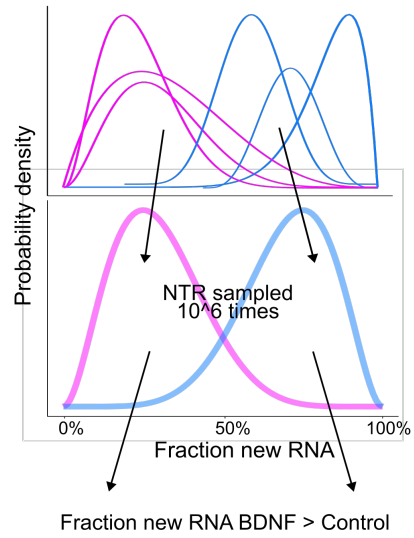

> 90% samples BDNF > Control	Higher new RNA
< 10% samples BDNF > Control	Lower new RNA
40% – 60% samples BDNF > Control	Equivalent new RNA

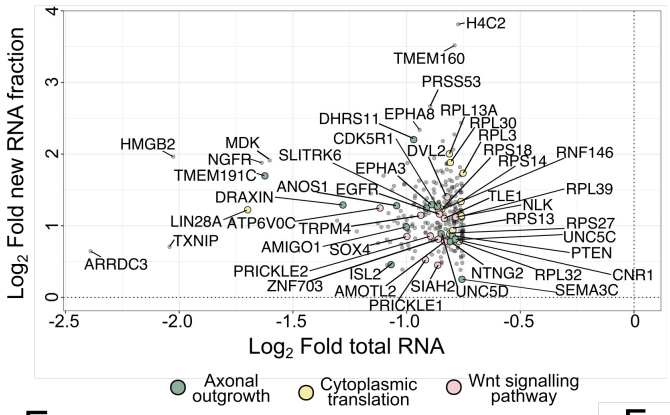

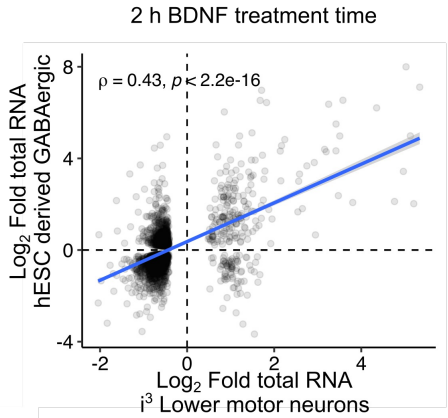

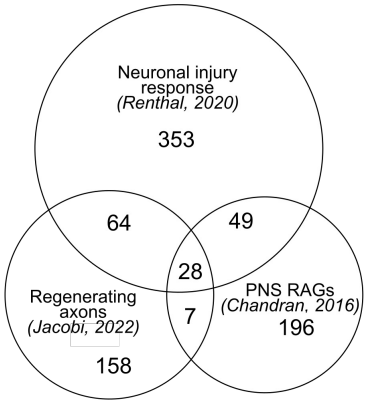

F

		Total RNA		New RNA	
	Time	NES	p.adjust	NES	p.adjust
Regenerating axons Jacobi, 2022	1	**1.744**	0.008367406	**1.450**	0.003937104
PNS RAGs Chandran 2016		2.482	0.0000000005	1.458	0.00376298670651763
Neuronal injury response Renthal, 2020		**1.904**	0.000156969	**1.497**	0.00000257
Regenerating axons Jacobi, 2022	2	**-1.617**	0.000195468	**1.282**	0.034188458
PNS RAGs Chandran 2016		**1.334**	0.04608782	1.088	0.29220779
Neuronal injury response Renthal, 2020		**-2.101**	0.0000000005	**1.243**	0.025097165
Regenerating axons Jacobi, 2022	6	**1.765**	0.000284161	1.291	0.066600067
PNS RAGs Chandran 2016		**2.085**	5.22338788724466E-08	1.121	0.31343656
Neuronal injury response Renthal, 2020		**1.776**	0.00000286	1.235	0.06660007

Fig 4. Global alterations of cytoskeletal-interacting proteins phosphorylation induced by BDNF in i³ LMNs

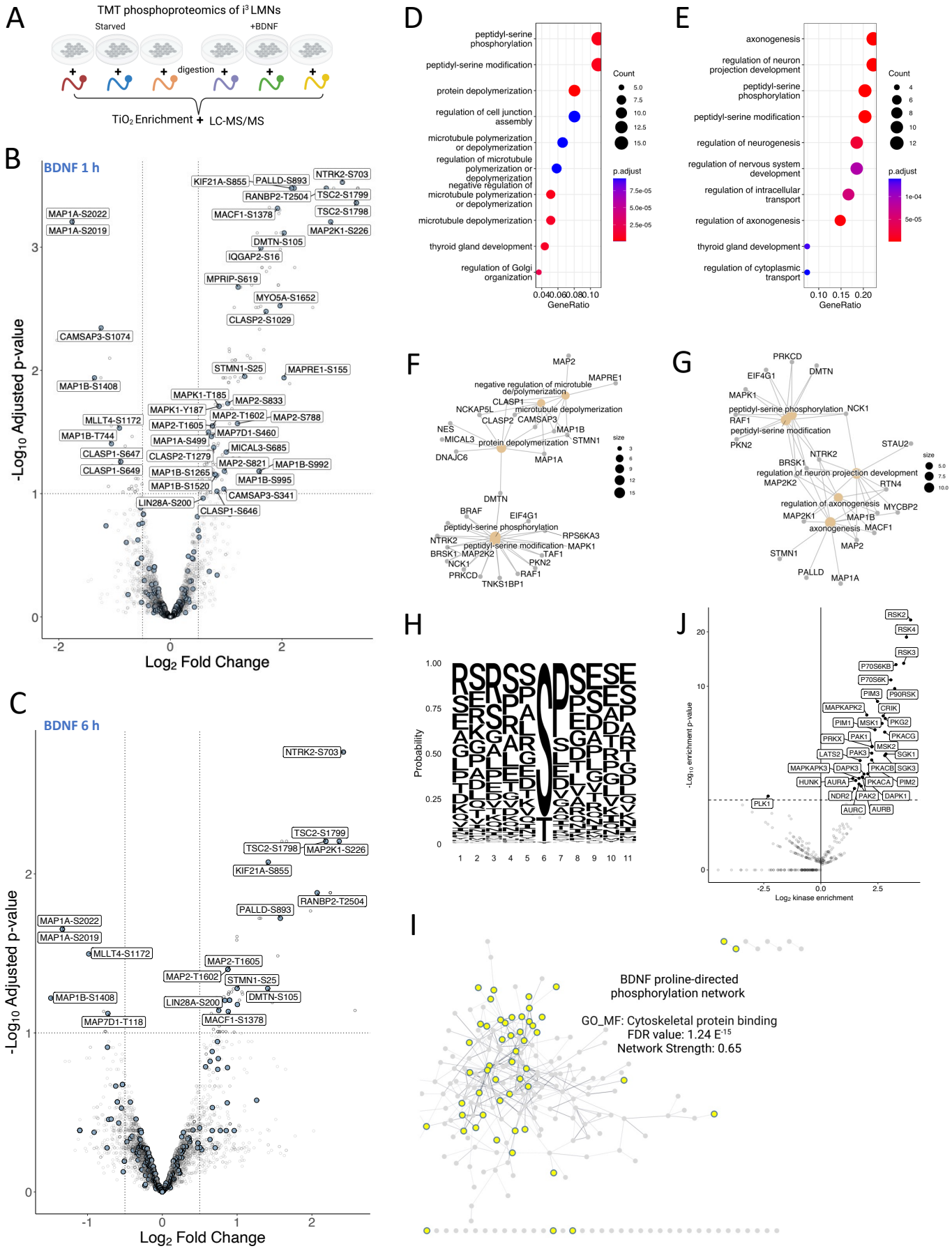

Fig S4. Microtubule- and actin-binding protein phosphorylation via BDNF in i^3 LMNs

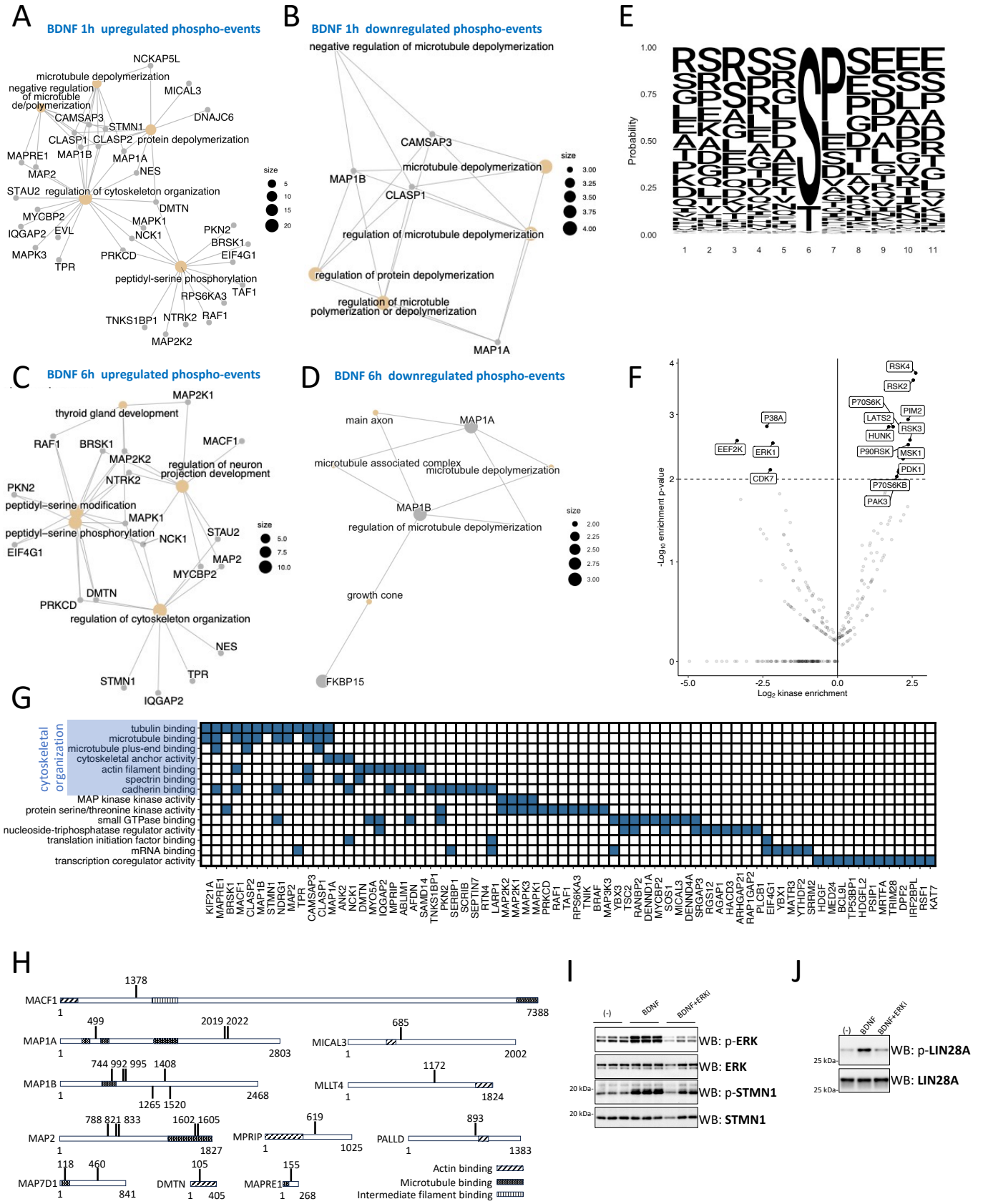

Figure 5. BDNF enhances retrograde transport and axonal regeneration through ERK1/2 in human motor neurons

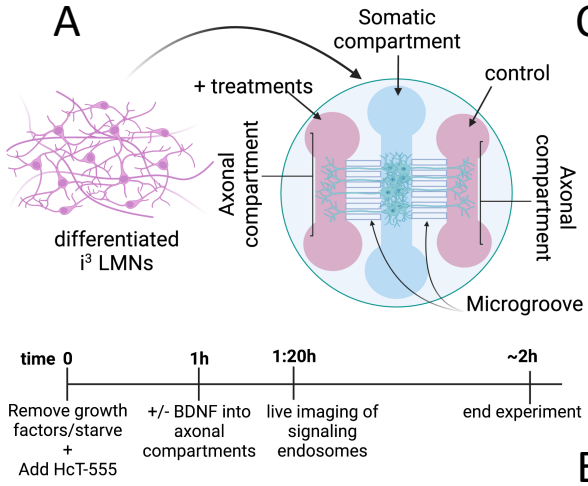

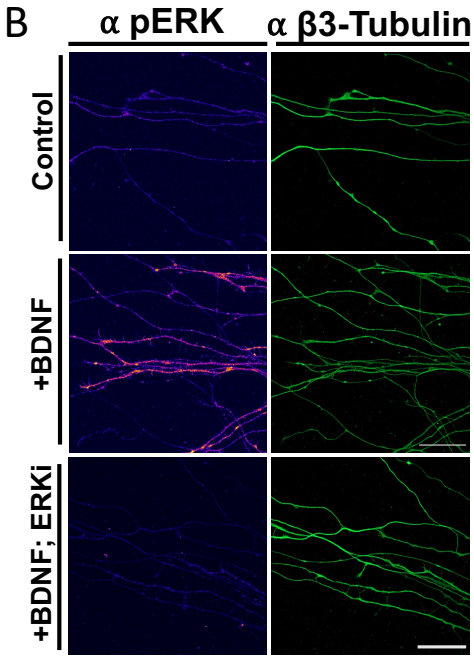

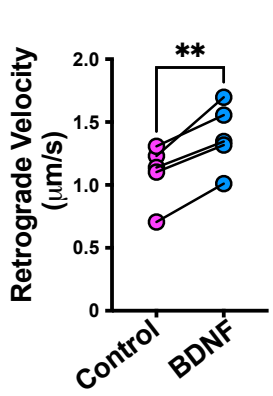

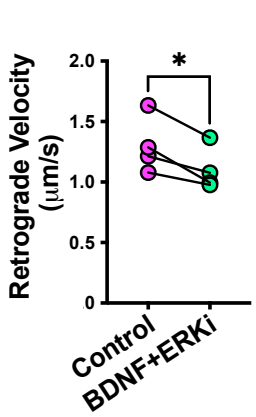

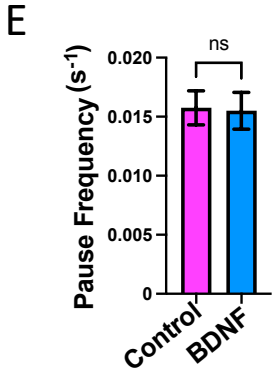

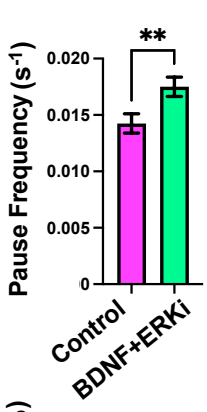

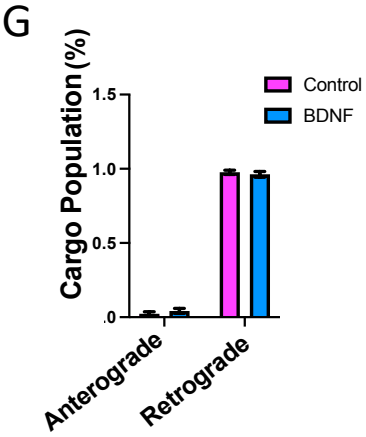

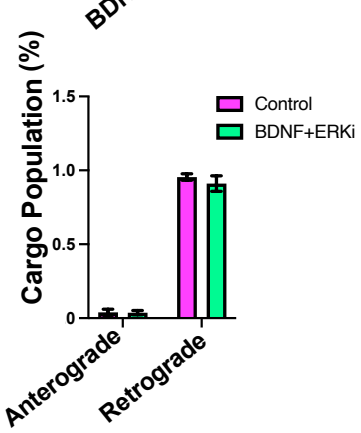

Fig. S5. BDNF and ERK1/2 regulates axonal transport of signaling endosomes in mice

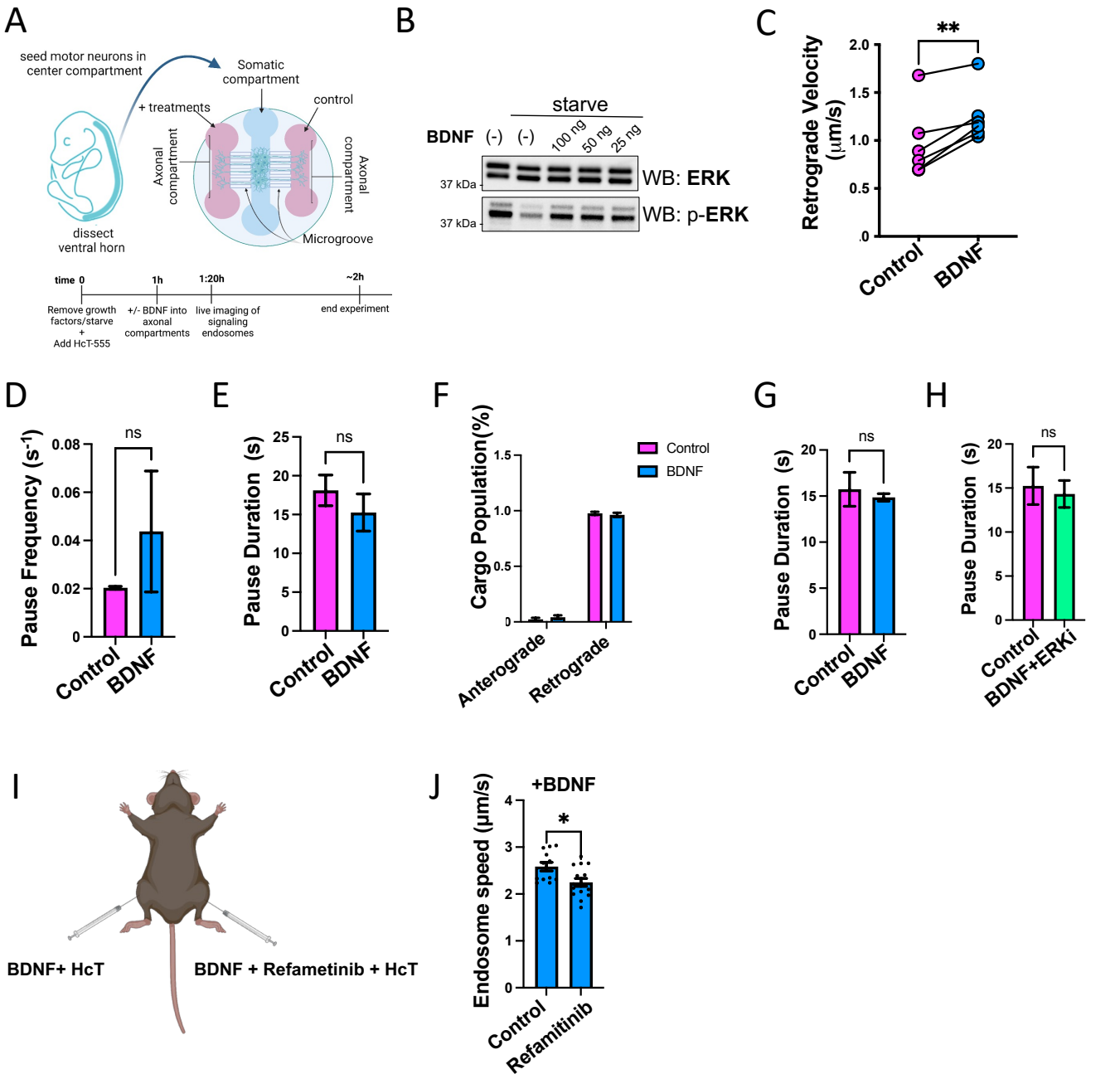

Figure 6. BDNF and ERK1/2 regulates axonal regeneration/outgrowth in i^3 LMNs

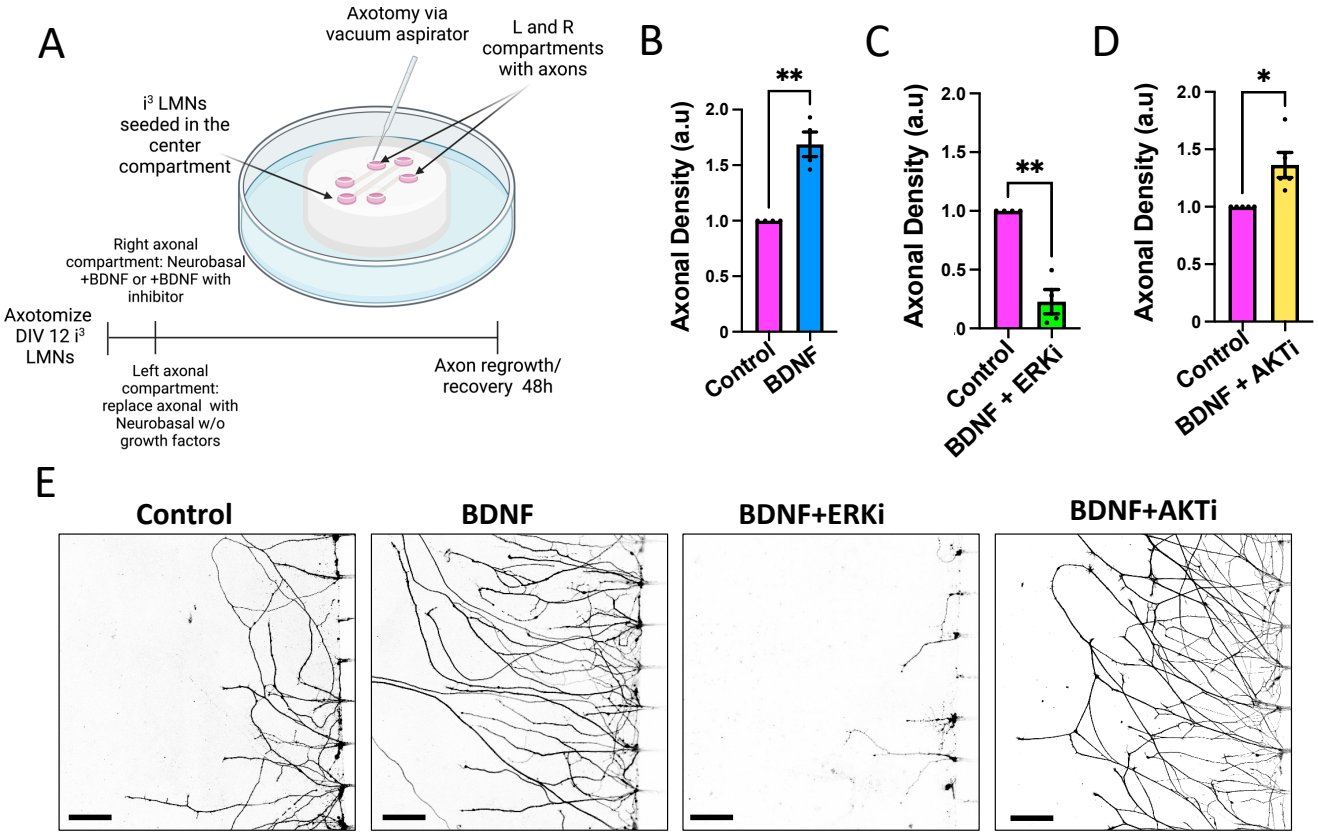
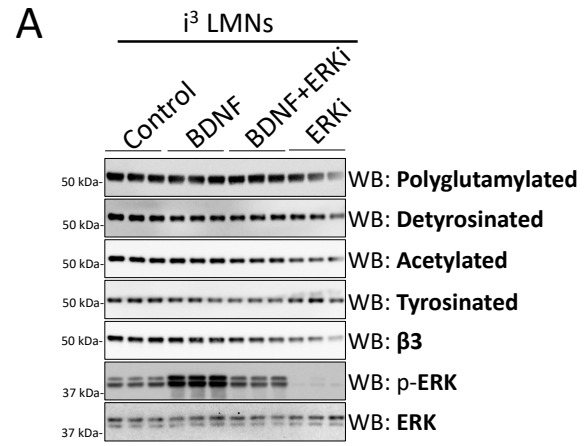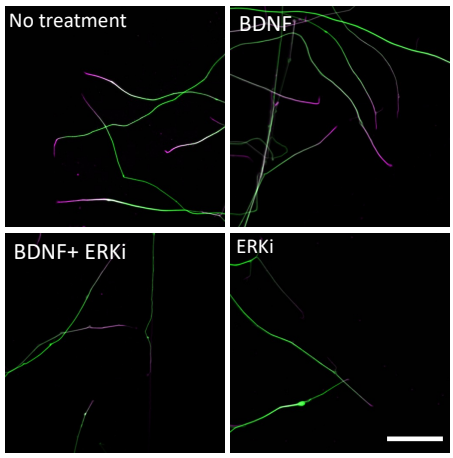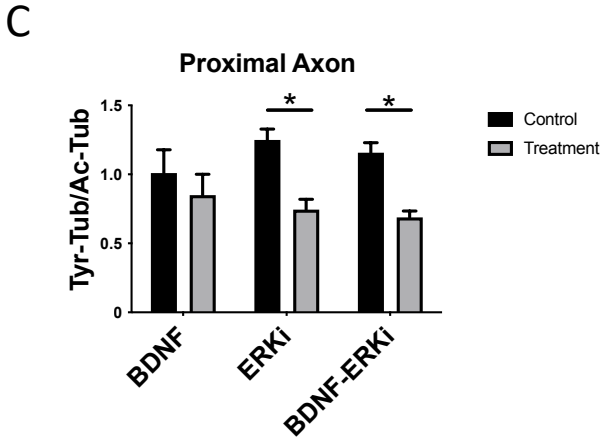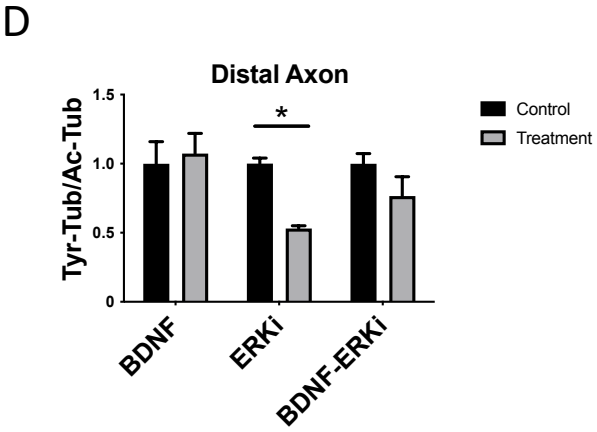
Figure S6. Microtubule modifications in i^{3}LMNs